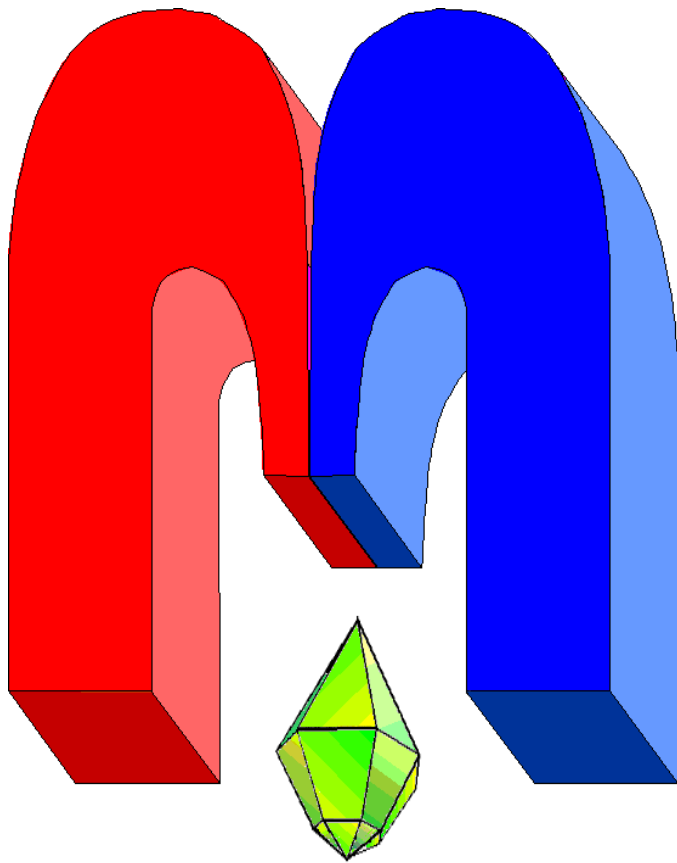


ISSN 2072-5981

doi: 10.26907/mrsej



***Magnetic
Resonance
in Solids***

Electronic Journal

Volume 23

Issue 2

Article No 21203

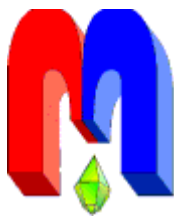
1-35 pages

2021

doi: [10.26907/mrsej-21203](https://doi.org/10.26907/mrsej-21203)

<http://mrsej.kpfu.ru>

<http://mrsej.ksu.ru>



Established and published by Kazan University*
Endorsed by International Society of Magnetic Resonance (ISMAR)
Registered by Russian Federation Committee on Press (#015140),
August 2, 1996
First Issue appeared on July 25, 1997

© Kazan Federal University (KFU)†

"Magnetic Resonance in Solids. Electronic Journal" (MRSej) is a peer-reviewed, all electronic journal, publishing articles which meet the highest standards of scientific quality in the field of basic research of a magnetic resonance in solids and related phenomena.

Indexed and abstracted by
Web of Science (ESCI, Clarivate Analytics, from 2015), Scopus (Elsevier, from 2012), RusIndexSC (eLibrary, from 2006), Google Scholar, DOAJ, ROAD, CyberLeninka (from 2006), SCImago Journal & Country Rank, etc.

Editor-in-Chief

Boris **Kochelaev** (KFU, Kazan)

Honorary Editors

Jean **Jeener** (Universite Libre de Bruxelles, Brussels)

Raymond **Orbach** (University of California, Riverside)

Executive Editor

Yurii **Proshin** (KFU, Kazan)
mrsej@kpfu.ru



This work is licensed under a [Creative Commons Attribution-ShareAlike 4.0 International License](https://creativecommons.org/licenses/by-sa/4.0/).



This is an open access journal which means that all content is freely available without charge to the user or his/her institution. This is in accordance with the [BOAI definition of open access](https://www.boai.ru/).

Technical Editor

Maxim **Avdeev** (KFU, Kazan)

Editors

Vadim **Atsarkin** (Institute of Radio Engineering and Electronics, Moscow)

Yurij **Bunkov** (CNRS, Grenoble)

Mikhail **Eremin** (KFU, Kazan)

David **Fushman** (University of Maryland, College Park)

Hugo **Keller** (University of Zürich, Zürich)

Yoshio **Kitaoka** (Osaka University, Osaka)

Boris **Malkin** (KFU, Kazan)

Alexander **Shengelaya** (Tbilisi State University, Tbilisi)

Jörg **Sichelschmidt** (Max Planck Institute for Chemical Physics of Solids, Dresden)

Haruhiko **Suzuki** (Kanazawa University, Kanazawa)

Murat **Tagirov** (KFU, Kazan)

Dmitrii **Tayurskii** (KFU, Kazan)

Valentine **Zhikharev** (KNRTU, Kazan)

* Address: "Magnetic Resonance in Solids. Electronic Journal", Kazan Federal University; Kremlevskaya str., 18; Kazan 420008, Russia

† In Kazan University the Electron Paramagnetic Resonance (EPR) was discovered by Zavoisky E.K. in 1944.

Two-pulse double quantum and five-pulse double-quantum modulation sequences in EPR: Coherence transfer and distance measurements

S.K. Misra*, H.R. Salahi

Physics Department, Concordia University, 1455 de Maisonneuve Boulevard West, Montreal, Quebec H3G 1M8, Canada

* *E-mail: sushil.misra@concordia.ca*

(Received August 24, 2021; revised November 3, 2021;
accepted November 3, 2021; published November 12, 2021)

Abstract. Double-quantum (DQ) coherence transfers and signals in two-pulse DQ and five-pulse DQM (double quantum modulation) pulsed EPR sequences, utilized for orientation selectivity and distance measurements in biological systems using nitroxide biradicals, have been calculated here for X-band (9.26 GHz) pulsed EPR (electron paramagnetic resonance) using a rigorous numerical algorithm. It is shown, in general, that both, a finite (selective) pulse, rather than an infinite (non-selective) pulse, and the dipolar interaction between the two nitroxide radicals, are needed to produce non-zero coherence transfers in $0 \rightarrow 2$ and $2 \rightarrow -1$ transitions. Furthermore, the simulations show that there exists orientational selectivity, as exhibited by the large value of the coherence transfer probability, $T_{0 \rightarrow 2}$, for those coupled nitroxides, whose dipolar axes, relative to the external magnetic field, are oriented symmetrically, within a small region, within about $\pm 10^\circ$ away from the magic angle $\theta = 54.74^\circ$ and its supplementary angle $\theta = 125.26^\circ$. It increases monotonically as the amplitude of the irradiation field (B_1) decreases. The magnitudes of the coherence transfers in the transitions $0 \rightarrow 2$ and $2 \rightarrow -1$ are found to be about the same. They depend upon both, the amplitude of B_1 and the duration of the pulse. As well, they increase significantly with increasing d , as found for $d = 10.0, 20.0, 30.0$ MHz, where $d = \frac{2}{3}D$, with D being the dipolar-coupling constant. The numerical calculations, using Monte-Carlo averaging, reveal that the Pake doublets occur at $\pm \frac{3}{4}d$ and $\pm d$ for the two-pulse DQ and the five-pulse DQM sequences, respectively, as calculated for $d = 0.5, 7.0, 10.0, 20.0, 30.0, 40.0, 50.0$ MHz. It is seen that for $d = 0.5$ MHz, considered here, for which the modulation depth can be measured within the dead-time, the dipolar depth of the modulation is $\approx 100\%$, which indicates that the DQ and DQM sequences are more efficient for distance measurements as compared to other techniques, e.g., DEER (double electron-electron resonance). The numerical algorithm for the five-pulse DQM sequence presented here is exploited to provide a good fit to the published experimental data. Simulations were also carried out at Ku-band (17.6 GHz), which showed that there occur no orientational selectivity at this band, unlike that at X-band. On the other hand, the signals and their Fourier transforms are found to be relatively more intense at Ku-band.

PACS: 76.30.-v, 76.70.Dx

Keywords: Pulsed EPR, distance measurements, double quantum (DQ), double quantum modulation (DQM), two-pulse DQ and five-pulse DQM, Liouville-von Neumann equation, stretched exponential, relaxation time measurements

1. Introduction

Multi-pulse EPR has been frequently exploited for distance measurements in biological systems using biradicals [1–13]. The details of rigorous numerical simulations for the four-, five-, and six-pulse DQC (double quantum coherence) sequences, which have been used for distance measurements in biological systems containing biradicals, were illustrated in detail in a recent publication by Misra and Salahi [14].

It is important to study coherence transfer from one coherent state, p , described by the differ-

ence in the magnetic quantum numbers $p = \Delta M_{rs}$, corresponding to the matrix element ρ_{rs} of the density matrix, to another coherent state $p' = \Delta M_{r's'}$, corresponding to the matrix element $\rho_{r's'}$ of the density matrix in pulsed-EPR (Electron Paramagnetic Resonance) experiments [15]. When $p = 0$ and $p' = 2$, this coherence transfer is known as double quantum (DQ) coherence and has been investigated frequently in NMR (nuclear magnetic resonance) [16–18]. However, unless $p = -1$, it does not lead to an observable magnetization. On the other hand, by transferring the $p = +2$ coherence to $p = -1$ coherence state by a subsequent coherence transfer, it can be observed, similar to that accomplished in NMR [19,20]. The advantage of exploiting DQ coherence is that the measured signal has a preferential sensitivity to the dipolar interaction, since the DQ transition is caused by the dipolar interaction. As a consequence, the extraction of distances from DQ coherence data, by estimating the value of d , where $d = \frac{2}{3}D$, with D being the dipolar-coupling constant, is cleaner than that obtained by other techniques. For example, in the frequently used DEER technique, one has to extract the weak dipolar echo modulation from the large echo decay background. As well, mono-radical impurities do not affect the DQ signal, unlike that in other techniques. The DQ method offers another advantage in that using it one can directly measure the double-quantum relaxation rate, T_2^D , the knowledge of which is very important to interpret motional dynamics.

This paper deals with a detailed study of coherence transfers in two-pulse DQ, as well as in five-pulse DQM, sequences in samples containing nitroxide biradicals as spin probes. The approach presented here can be applied to study the structural characterization of co-doped paramagnetic centers [21] as well as electron-nuclear and electron-electron transitions for quantum computing [22–26], involving the dipolar interaction between two paramagnetic ions. The numerical simulations exploited here to calculate DQ and DQM signals for X-band (9.26 GHz) pulsed EPR, corresponding to the experimental data reported in [3], consider the dipolar interaction between the two nitroxide dipoles of the biradical, as well as the fully asymmetric g and hyperfine matrices, and the angular geometry of the biradical, following the same algorithm as that used in [14]. It is noted that DQM is an elaboration of the two-pulse DQ sequence by introducing a refocusing π -pulse to enhance the signal. Among others, this paper is focused on investigating how to make the $p = 0$ to $p = +2$ DQ transition possible, which is forbidden for a non-selective (hard) pulse, by using a finite pulse in the presence of the dipolar interaction between the two nitroxides of the biradical [27]. In addition, the important role the DQ transition plays in pulsed EPR will be discussed, demonstrating the high sensitivity of the 2D-DQ EPR signals to the strength of the dipolar interaction for $d = 0.5, 7.0, 10.0, 20.0, 30.0, 40.0, 50.0$ MHz and how to exploit it to calculate the dependence of orientational selectivity upon the orientation of the dipolar axis of the biradicals. It is noted that present studies are only carried out for $0.5 \text{ MHz} \leq d \leq 50.0 \text{ MHz}$, because for $d < 0.5 \text{ MHz}$, not enough cycles of the dipolar modulation of the signal are observed in the window of observation of $7 \mu\text{s}$, whereas the pulse EPR technique is not suitable to measure distances corresponding to $d > 50 \text{ MHz}$ ($r \approx 10 \text{ \AA}$) [2]. The separation of Pake doublets provides a direct measure of the dipolar interaction, from which the distance between the two nitroxide dipoles in the nitroxide biradical used as spin probe, can be determined, by using the expression that relates the distance in \AA to the dipolar constant d , expressed in MHz: $r = 10 (52.04 \text{ MHz}/d)^{1/3} \text{ \AA}$, where d is the dipolar-coupling constant. The simulations, as carried out here for a fixed value of r , can be exploited to calculate the signal for a distribution of r , if required, when the probabilities for distance distribution are available.

A thorough and complete calculation of DQ and DQM time-dependent signals for the polycrystalline (powder) samples using Monte-Carlo averaging over random orientations of the respective Euler angles of the two nitroxide dipoles with respect to the dipolar axis, needed to calculate the Pake doublets from their Fourier transforms, will be carried out here using Matlab. To this end, full numerical diagonalizations of the pulse- and/or spin-Hamiltonian matrices will be carried out, and the two-pulse DQ and five-pulse DQM signals will be calculated exploiting the algorithm developed in Misra *et al.* [2]. In addition, five-pulse DQM EPR signal will be exploited to fit the experimental data reported by Saxena *et al.* [28]. The effect of relaxation on the powder averages will be considered here by multiplying the final signal with a stretched exponential [29, 30]. Furthermore, it will be shown here, from general considerations, that a finite, rather than a non-selective pulse, in conjunction with the dipolar interaction, is needed to produce non-zero $0 \rightarrow 2$ and $2 \rightarrow -1$ coherence transfers in the DQ experiment. In addition, analytical expressions required will be derived here for coherence transfers, using *Mathematica*, for two-pulse DQ and five-pulse DQM signals for an arbitrary orientation of the external magnetic field with respect to the dipolar axis.

The organization of this paper is as follows. Section 2 deals with the general theoretical details, including the static and pulse-Hamiltonians for the nitroxide biradical and the solution of Liouville von Neumann equation to calculate the signal. The procedure for a rigorous numerical calculation of the coherence transfers $T_{0 \rightarrow 2}$ and $T_{2 \rightarrow -1}$ is given in Sec. 3, whereas Sec. 4 deals with the numerical algorithm to simulate the DQ and DQM signals rigorously for a polycrystalline sample in the absence of relaxation. The Orientational selectivity in two-pulse DQ and five-pulse DQM signals is discussed in Sec. 5. Considering relaxation in a polycrystalline sample, using a stretched exponential, is discussed in Sec. 6. The effect of the dead-time after the application of the last pulse, during which the signal is not observable, on the modulation depth is discussed in Sec. 7. In Sec. 8, the numerical results of the various simulations for the DQ and DQM sequences are presented. The conclusions are summarized in Sec. 9.

2. Theoretical Details

This section deals with the theory and the procedure to calculate the two-dimensional (2D) EPR signal for a coupled nitroxides biradical. One considers here two dipolar-interaction coupled nitroxides, each characterized by an electron with spin $S = 1/2$ and a nucleus with spin $I = 1$. The dimension of the Hilbert space, in which the present calculations will be carried out, for such a system is 36×36 , since $(2S_1 + 1)(2S_2 + 1)(2I_1 + 1)(2I_2 + 1) = 36$, where the indices 1, 2 refer to the two nitroxide.

2.1. Static Spin Hamiltonian

For the coupled nitroxides the spin Hamiltonian in the rigid limit, valid for a sample in the frozen state, is [1, 2]

$$H_0 = H_{01} + H_{02} + H_{12}, \quad (1)$$

where H_{0k} ; $k = 1, 2$, denote the static Hamiltonians of the two nitroxide radicals, including the Zeeman and hyperfine interactions. Assuming the respective g and hf matrices of each nitroxide to have coincident principal-axis systems, the effective H_{0k} is expressed as

$$H_{0k} = C_k S_{z_k} + A_k S_{z_k} I_{z_k} + B_k S_{z_k} I_{+k} + B_k^* S_{z_k} I_{-k}; \quad k = 1, 2. \quad (2)$$

In Eq. (1), S_{z_k} , I_{z_k} , I_{+k} and I_{-k} are the spin operators for the two nitroxides, and the expressions for the coefficients C_k , A_k and B_k are given in [14]. It is noted that, in writing Eq. (2), the nuclear

Zeeman and nuclear quadrupole interactions are neglected, as is appropriate for nitroxides in magnetic fields of 3.3 kG, corresponding to the X-band frequency, considered here. H_{12} in Eq. (1) includes the dipolar and exchange coupling between the two nitroxide radicals, expressed as

$$H_{12} = \frac{D}{2} (3 \cos^2 \theta - 1) (S_z^2 - \mathbf{S}^2/3) + J \left(\frac{1}{2} - 2 \mathbf{S}_1 \mathbf{S}_2 \right), \quad (3)$$

where θ is the polar angle of the orientation of the static magnetic field with respect to the

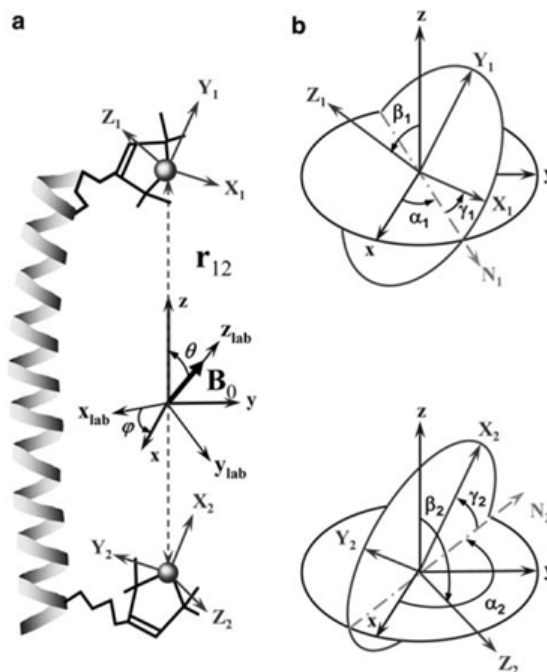


Figure 1. (a) The two nitroxides in the biradical in the dipolar frame of reference. The z -axis of the dipolar frame is chosen to be along the vector \mathbf{r}_{12} connecting the magnetic dipoles of the nitroxides. The relative orientation of the laboratory-fixed frame (with its z_{lab} axis along the external magnetic field B_0) and the dipolar frame is defined by the Euler angles $\eta = (0, \theta, \phi)$ (b) The set of Euler angles $\lambda_k = (\alpha_k, \beta_k, \gamma_k)$, ($k = 1, 2$), which define the orientations of the hyperfine and g -matrix principal axes for nitroxides 1 and 2 in the dipolar frame with respect to molecular frame of reference (denoted by X_k, Y_k, Z_k , $k = 1, 2$); here N_1 and N_2 are the lines of nodes for the two nitroxide frames. For the numerical calculations in the present work, the x axis of the first nitroxide magnetic frame is chosen to be along the line of nodes of the first nitroxide, N_1 , so the value of α_1 becomes zero. (This figure is reproduced from [2] by permission.)

dipolar axis that connects the magnetic dipoles of the two nitroxides, as shown in Fig. 1 and $\mathbf{S} = \mathbf{S}_1 + \mathbf{S}_2$ is the total electron spin. In Eq. (3), J is the exchange-interaction constant between the two electrons, and D is the strength of the dipolar interaction, expressed in terms of r , the distance between nitroxides, as [1, 2].

$$D = \frac{3 \gamma_e^2 \hbar}{2 r^3}, \quad (4)$$

where γ_e is the gyromagnetic ratio of the electron and $\hbar = h/2\pi$ is the reduced Planck's constant. The constant $d = 2D/3$ will be used hereafter, referred to as the ‘‘dipolar constant’’. (It is noted that the analytical expressions for the energy levels of a radical pair, consisting of electron-nuclear spin-coupled systems, were derived, for a general case, for arbitrary values of g - and hyperfine matrices, zero-field splitting terms, dipolar interaction, and exchange interaction

between electrons spins by Itoh *et al.* [31]. However, in the numerical simulations over a powder, use of these expressions is not efficient.)

The magnetic basis, described by the basis-vectors $|M_{S_1}, M_{S_2}, m_{I_1}, m_{I_2}\rangle$, is used hereafter, where $M_{S_1}, M_{S_2}, m_{I_1}, m_{I_2}$ denote the two electronic and the two nuclear magnetic quantum numbers, respectively, for the two nitroxides.

2.2. Initial density matrix.

To calculate the signal for a multi-pulse sequence, one starts with the initial density matrix, ρ_0 , governed by the Boltzmann distribution for two electrons, each with spin 1/2, in thermal equilibrium. Using the high-temperature approximation and neglecting the energy-level modification by the hyperfine interaction, which is much less than the electronic Zeeman interaction, one can write:

$$\rho_0 = \frac{\exp(-H_0/kT)}{\text{Tr}[\exp(-H_0/kT)]} \propto \mathbb{1} - \frac{\hbar\omega_0}{k_B T} S_Z + \dots \quad (5)$$

Since the final signal is obtained by taking the trace: $\text{Tr}(S_+ \rho_f)$ and during the evolution of ρ_0 to ρ_f the term $\mathbb{1}$ remains invariant, it does not contribute to the signal as $\text{Tr}(S_+ \mathbb{1}) = 0$. One can then replace ρ_0 , for the calculation of the signal, as follows:

$$\rho_0 \rightarrow S_Z = S_{z_1} + S_{z_2}. \quad (6)$$

2.3. Calculation of the effect of pulse

During the application of a pulse, the spin relaxation is here neglected as it has negligible effect, since the durations of the pulses are much smaller than the relaxation time. In that case, the evolution of the density matrix is described in Hilbert space, as follows:

$$\frac{d}{dt}\rho(t) = -i[(H_0 + H_p), \rho(t)], \quad (7)$$

with H_p being expressed as [1, 2]:

$$H_p = \frac{\omega_1}{2} \left(e^{-i\phi} S_+ + e^{i\phi} S_- \right), \quad (8)$$

where $B_1 = \omega_1/\gamma_e$ is the amplitude of the pulse, ϕ is the phase of the pulse and S_{\pm} are the raising/lowering operators of the total electronic spin of the coupled nitroxide system in the 36×36 direct product Hilbert space:

$$S_{\pm} = S_{\pm S_1} \otimes \mathbb{1}_{S_2} \otimes \mathbb{1}_{I_1} \otimes \mathbb{1}_{I_2} + \mathbb{1}_{S_1} \otimes S_{\pm S_2} \otimes \mathbb{1}_{I_1} \otimes \mathbb{1}_{I_2}, \quad (9)$$

where \otimes stands for the direct product, S_{\pm} are expressed in terms of the Pauli matrices σ_x and σ_y as $S_{\pm} = \frac{1}{2}(\sigma_x \pm i\sigma_y)$; $\mathbb{1}_{S_k}$ and $\mathbb{1}_{I_k}$; $k = 1, 2$ are identity matrices in the electronic 2×2 and nuclear 3×3 spaces, respectively, of the two nitroxides. The tip angle, β , expressing spin rotation by the pulse is expressed as:

$$\beta = \gamma_e B_1 t_p, \quad (10)$$

where t_p is the duration of the B_1 field.

2.4. Calculation of multi-pulse EPR signal

The pulsed EPR signal for the system of coupled nitroxides, undergoing spin relaxation, is calculated by solving Liouville von-Neumann (LVN) equation that governs the time evolution of the density matrix during free evolution, i.e., in the absence of a pulse. It is expressed as [1–14]

$$\frac{d}{dt}\chi(t) = -i[H_0, \chi(t)] + \hat{\Gamma}\chi(t), \quad (11)$$

where $\chi = \rho - \rho_0$ is the reduced density matrix, with $\rho_0 \propto S_{z_1} + S_{z_2}$, being the initial density matrix, as discussed in Sec. 2.2, and H_0 is given by Eq. (1). In Eq. (11), $\hat{\Gamma}$ is the relaxation superoperator in Liouville space. In accordance with Saxena and Freed [1], a simplified one with the following matrix elements is chosen here:

$$\hat{\Gamma}_{ij,kl} = -\delta_{ij}\delta_{kl}\frac{1}{(T_1)_{ik}} - \delta_{ik}\delta_{jl}(1 - \delta_{ij})\frac{1}{T_2^{S,D}}, \quad (12)$$

where $(T_1)_{ik}$ are the spin-lattice relaxation times between the populations ii to kk , which are operative on the coherence pathway $p = 0$, and $T_2^{S,D}$ are the spin-spin relaxation times operative along the $p = \pm 1$ (index S), and $p = \pm 2$ (index D) pathways, as shown in Fig. 2. It is noted that, in general, the spin-spin relaxation times, $(T_2^{S,D})_{ij}$ are different for different transitions ij , but these relaxation times are only slightly different from each other as shown in [32, 33]. As a consequence, they are all approximated here in Eq. (12) to have the same average spin-spin relaxation time $T_2^{S,D}$.

In the two-pulse DQ sequence, shown in Fig. 2(a), the pathway $p = 0$ is excluded, so that the relaxation times $(T_1)_{ik}$, with $i = k$, affecting the populations, that appear in Eq. (12) for the $p = 0$ pathway, have no effect on the signal. In the two-pulse sequence considered here, only the coherence pathways $p = +2$ and $p = -1$ participate, so that in the relaxation only the second term on the right-hand side of Eq. (11) which corresponds to $i \neq j$ elements of the reduced density matrix, affect the two-pulse DQ signal. Then, the solution of Eq. (11) after time t , expressing the evolution of χ_{ij} due to the relaxation along the $p = \pm 1, \pm 2$ pathways, is obtained as

$$\chi(t_0 + t) = e^{-t/T_2^{S(D)}} e^{-iH_0 t} \chi(t_0) e^{iH_0 t}. \quad (13)$$

The elements of the matrix for $e^{-iH_0 t}$ used in Eq. (13) for the coupled nitroxides system are given in [14].

As for the five-pulse DQM signal, which includes the coherence pathway $p = 0$ (Fig. 2(b)), one also needs to consider the relaxation between the populations. To do that rigorously, one first needs to diagonalize the non-diagonal part of the relaxation matrix in Liouville space, as given by Eq. (12), which is a 36×36 matrix. At lower temperatures, used in the five-pulse experiment, the values of the off-diagonal elements of the relaxation matrix $(T_1)_{ik}$ in Eq. (11) for $i \neq k$, are larger than both the spin-spin relaxation times and the duration of the experiment by two order of magnitudes [33]; hence $e^{-t/(T_1)_{ik}} \approx 1$, so they do not have any significant effect on the final signal and can thus be neglected. Keeping now only the diagonal elements of the relaxation matrix and assuming that they are all equal to each other [32, 33], the time evolution of the reduced density matrix on the coherence pathway $p = 0$ is approximates as:

$$\chi(t_0 + t) = e^{-t/T_1} e^{-iH_0 t} \chi(t_0) e^{iH_0 t}. \quad (14)$$

The solution of Eq. (7), after the application of a pulse of duration t_p , neglecting relaxation during the pulse, is given as [1]:

$$\rho(t_0 + t_p) = e^{-i(H_0 + H_p)t_p} \rho(t_0) e^{i(H_0 + H_p)t_p}. \quad (15)$$

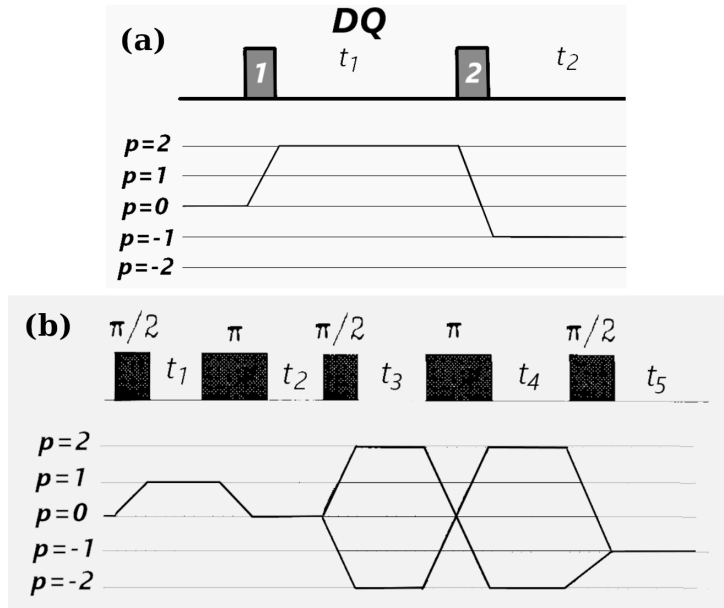


Figure 2. The pulse schemes and the relevant coherence pathways for (a) two-pulse DQ sequence; (b) five-pulse DQM sequence. The time intervals (t_i ; $i = 1, 2$ for DQ and $i = 1, 2, 3, 4, 5$ for DQM) between the pulses, as well as after the last pulse for the two sequences are indicated. Here p is the coherence order, which represents the transverse magnetization, corresponding to the spins rotating in the plane perpendicular to the external field.

After the application of a pulse, the density matrix is projected onto the coherence pathway of interest, which are: $p = 2, -1$ for DQ and $+1, 0, \pm 2, \mp 2, -1$ for DQM sequences, respectively, as given in Fig. 2. This is achieved by the use of a projection operator matrix that retains only the relevant elements of the density matrix which correspond to a particular pathway, p , putting all the other elements equal to zero by making a Hadamard product. The projection-operator matrices for the various coherence pathways are given in [14].

For the calculation of two-pulse DQ signals, the final density matrix $\rho_f(t_1, t_2)$, where t_1 is the time between the two pulses and t_2 is the time after the second pulse, at which the signal is recorded, as shown in Fig. 2(a), is obtained as follows. (i) Transform the initial density matrix by the first pulse using Eq. (15); (ii) Apply, the projection operator i.e., take the Hadamard product, of the relevant coherence pathway projection operator matrix with the density matrix transformed in step (i); (iii) Calculate the density matrix after free evolution with relaxation of the density matrix obtained in step (ii) over the duration t_1 between the first and the second pulses using Eq. (13); (iv) Transform the density matrix obtained in step (iii) by the second pulse using Eq. (15); (v) Apply the coherence pathway projection operator matrix for the coherence pathway $p = -1$ to the density matrix obtained in step (iv); (v) the final density matrix $\rho_f(t_1, t_2)$ is obtained after free evolution with relaxation of the density matrix obtained in step (iv) over the time t_2 .

For the five-pulse DQM, signals, the final density matrix $\rho_f(t_1, \dots, t_5)$ with t_k ; $k = 1, \dots, 5$ being the time between the k th and $(k + 1)$ th pulse is obtained by successive applications of the 5 pulses to the initial density matrix, using Eq. (15), followed by the application of the relevant coherence pathway projection operator matrix and then free evolution over the coherence pathways as shown in Fig. 2(b), using Eqs. (13) and (14) for the coherence pathways $p = \pm 1, \pm 2$ and $p = 0$, respectively.

The complex signal, for the orientation, (θ, ϕ) , of the static magnetic field relative to the

dipolar axis that connects the magnetic dipoles of the two nitroxides for the orientation of the two nitroxide radicals with respect to the molecular frame, characterized by six Euler angles, $\{\alpha_1, \beta_1, \gamma_1, \alpha_2, \beta_2, \gamma_2\}$, as shown in Fig. 1, is then,

$$S^{(k)}(\{\mathbf{t}_k\}, \theta, \phi, \beta_1, \gamma_1, \alpha_2, \beta_2, \gamma_2) = \text{Tr}(S_+ \rho_f \{\mathbf{t}_k\}), \quad (16)$$

where $\{\mathbf{t}_k\}$, $k = 2, 5$ stand for t_1, t_2 and t_1, t_2, t_3, t_4, t_5 for the calculation of two-pulse and five-pulse signals, respectively. It is noted that, of the six Euler angles, only five are independent and one is arbitrary which can be chosen to be 0 e.g., α_1 . This is achieved by choosing the x axis along the line of nodes, N_1 , of the first nitroxide (Fig. 1).

Polycrystalline average. The EPR signal for a polycrystalline sample is calculated by integrating Eq. (16) over (θ, ϕ) covering the unit sphere. The numerical calculations of the DQ and DQM signals in the present work were performed over the quadrant: $\theta = [0, \pi/2]$ and $\phi = [0, \pi]$, following Misra, Borbat and Freed [2], since the spin Hamiltonian coefficients of the coupled nitroxide system, which are specifically $A_1, B_1, C_1, A_2, B_2, C_2$, have the following symmetry for a chosen set of Euler angle ($\alpha_1 = 0, \beta_1, \gamma_1, \alpha_2, \beta_2, \gamma_2$): In the transformation $\phi \rightarrow 2\pi - \phi$, in going from the first quadrant to the second quadrant, it is found that $A_1 \rightarrow A_1, B_1 \rightarrow B_1^*, C_1 \rightarrow C_1, A_2 \rightarrow A_2, B_2 \rightarrow B_2^*, C_2 \rightarrow C_2$, where $*$ indicates the complex conjugate. In other words, the value of spin Hamiltonian coefficients A_1, C_1, A_2, C_2 for a chosen value of (θ, ϕ) in the first quadrant: $0 \leq \theta \leq \pi/2$ and $0 \leq \phi \leq \pi$, is the same as that for $(\theta, 2\pi - \phi)$, which covers the second quadrant: $(0 \leq \theta \leq \pi/2$ and $\pi \leq \phi \leq 2\pi)$. As for the spin Hamiltonian coefficients B_1, B_2 , which become complex conjugated in the second quadrant when $(\theta, \phi) \rightarrow (\theta, 2\pi - \phi)$, it is noted that the final signal depends on the eigenvalues and eigenvectors of the spin Hamiltonian rather than the spin Hamiltonian coefficients per se. As seen from Eqs. (B.3) and (B.10) of [14], which state the eigenvectors and eigenvalues for the coupled nitroxide system, respectively, only the absolute values $|B_1|, |B_1|^2, |B_2|, |B_2|^2$ appear, which indicate that the signal calculated for (θ, ϕ) in the first quadrant is the same as that in the second quadra $(\theta, 2\pi - \phi)$. Furthermore, this symmetry was confirmed numerically by integrating the DQ signal over the first quadrant and the hemisphere, consisting of the first and second quadrants for two cases which are specifically Figs. 4b₁, 4b₂, 4c₁, 4c₂. The same average values of the signal per orientation over the first quadrant and the hemisphere, consisting of the first and second quadrants, are found in each case. So, it suffices to carry out the integral only over the first quadrant of the unit sphere as follows [34]

$$S^{(k)}(\{\mathbf{t}_k\}, \lambda_1, \lambda_2) = 4 \int_0^\pi d\phi \int_0^{\pi/2} S^{(k)}(\{\mathbf{t}_k\}, \eta, \lambda_1, \lambda_2) d(\cos \theta); \quad k = 2, 5. \quad (17)$$

In Eq. (17) the set of Euler angles, $(\alpha_1 = 0, \beta_1, \gamma_1); (\alpha_2, \beta_2, \gamma_2)$, and the orientation of the external magnetic field with respect to the dipolar axis (θ, ϕ) are denoted, respectively, as $\lambda_j; (j = 1, 2)$ and η . In the present work, the distance between the two nitroxide fragments is considered to be fixed and the orientations of the Euler angles $(\beta_1, \gamma_1, \alpha_2, \beta_2, \gamma_2)$ for the polycrystalline sample are chosen completely random.

Calculation of Pake doublets. For this, one needs to average over the Euler angles λ_1, λ_2 , the orientations of the dipoles of the two nitroxides. This is an enormous task as there are infinite many such possibilities. However, one can, instead, use Monte-Carlo averaging, wherein one varies λ_1, λ_2 randomly as follows:

$$S_{avg}^{(k)}(\{\mathbf{t}_k\}) = \sum_{\lambda_1, \lambda_2} S^{(k)}(\{\mathbf{t}_k\}, \lambda_1, \lambda_2). \quad (18)$$

Twenty such averaging were found to be sufficient here, because another set of twenty Monte-Carlo averaging gave almost identical results.

Inhomogeneous Gaussian broadening due to precession of spins during the free evolution. In order to take into account the Gaussian inhomogeneous broadening effect, the final signals $S(\mathbf{t}_k)$ in Eq. (18) for each orientation (θ, ϕ) are multiplied by the by the factors $e^{-2\pi^2\Delta_G^2(t_2-2t_1)^2}$ for two-pulse DQ [1] and $e^{-2\pi^2\Delta_G^2(t_5-t_1)^2}$ for five-pulse DQM, where Δ_G is the Gaussian inhomogeneous broadening parameter.

Number of simulations. A grid of 90 θ -values and 90 ϕ -values were used over a unit sphere for one simulation. These simulations were repeated for 20 sets of five independent Euler angles (λ_1, λ_2) to calculate the Pake doublet, representing an average over random orientation of the two nitroxide dipoles. This amounts to an average over $90 \times 90 \times 20 = 1.62 \times 10^5$ simulations. The procedure to calculate the two-pulse DQ and five-pulse DQM signal is described in the flowchart in Appendix A.

2.5. Analytical expressions of two-pulse DQ and five-pulse DQM:

One-dimensional signals

Analytical expressions of the signals are useful in deducing important features of the signal and its Fourier transform. In this section, the analytical expression for two-pulse DQ and five-pulse DQM one-dimensional signals i.e., the signal calculated at the top of the echo, are expressed, following the general algorithm to calculate the analytical expression of pulsed EPR signal given in [14].

2.5.1. One-dimensional two-pulse DQ signal

The pulse sequence for the DQ sequence is shown in Fig. 2(a). It consists of two finite arbitrary pulses with the same duration, t_p . The phase cycling required for the pathways $p = 2$ and $p = -1$ in the two-pulse DQ sequence is given in Table II of [1]. The echo in this pulse sequence occurs at $t_{echo} = t_2 = 2t_1$ [1]. Using the same approximations to calculate the analytical expressions of the pulsed EPR signals as in [14], the 1D signal for two-pulse DQ sequence i.e., at $t_2 = 2t_1$, is expressed as

$$\begin{aligned} \text{DQ}^{Signal}(t_2) = & e^{i(3\phi_2-2\phi_1)} e^{-t_2/(1/2T_2^D+1/T_2^S)} \text{Tr} \left[\left(P_{11}^{(1)} P_{41}^{(1)\dagger} - P_{14}^{(1)} P_{44}^{(1)\dagger} \right) \right. \\ & \left. \times \left\{ \left(P_{24}^{\dagger} + P_{34}^{\dagger} \right) P_{41}^2 e^{-i\frac{3}{4}d \times (3 \cos^2 \theta - 1)t_2} + P_{14}^{\dagger} \left(P_{21}^2 + P_{31}^2 \right) e^{+i\frac{3}{4}d \times (3 \cos^2 \theta - 1)t_2} \right\} \right], \end{aligned} \quad (19)$$

where ϕ_1 and ϕ_2 are the phase of the first and second pulses, respectively, and the trace is taken over the 9×9 hyperfine space [14]. The P_{ij}^k , $i = 1, \dots, 4$; $j = 1, 4$; $k = 1, 2$ terms in Eq. (19) are 9×9 matrices in the hyperfine space, as given in [14]. An examination of Eq. (19) reveals that the signal depends on $\pm \frac{3d}{4} \times (3 \cos^2 \theta - 1)t_2$, whose Fourier transform, as a function of t_2 , would yield peaks at the frequencies $\pm \frac{3d}{4} \times (3 \cos^2 \theta - 1)$ for any choice of the five independent Euler angles. This leads to the conclusion that the Pake doublets occur at $\pm \frac{3d}{4}$, when averaged over the orientations of the two nitroxide dipoles over the unit sphere.

2.5.2. One-dimensional five-pulse DQ signal

The five-pulse DQM pulse sequence is shown in Fig 2(b), wherein the fourth pulse, $(\pi)_x$, plays the role of a refocusing pulse. In the experiment, $t_1 = t_2$, which are stepped and, $t_3 = t_4$, which

Coherence transfer and distance measurements

are fixed and will here be denoted as $t_{\text{DQ}}^{(\text{DQM})}$. The echo in this five-pulse DQM sequence occurs at the time $t_{\text{echo}} = t_5 = t_1$.

The five-pulse DQM sequence, shown in Fig. 2(b), is tantamount to two coherence pathways, both of which lead to the formation of an echo at $t_5 = t_1$. These are:

$$\begin{aligned} \text{(i)} \quad & p = 0 \rightarrow +1 \rightarrow 0 \rightarrow +2 \rightarrow -2 \rightarrow -1; \\ \text{(ii)} \quad & p = 0 \rightarrow +1 \rightarrow 0 \rightarrow -2 \rightarrow +2 \rightarrow -1. \end{aligned} \quad (20)$$

In the analytical calculations here, finite pulses are used to effect the transitions $1 \rightarrow 0$ and $0 \rightarrow \pm 2$, otherwise for the remaining pathways strong pulses are used, which do not require inclusion of H_0 , so that $H_p \gg H_0$.

Following the procedure described in [14], the 1D five-pulse DQM signals for the two coherence pathways in Eq. (20) are calculated for $t_1 = t_5$, for the orientation of the dipolar axis, oriented at an angle θ with respect to the external magnetic field (lab frame), indicated by the superscripts (i) and (ii), respectively, to be as follows:

$$\begin{aligned} \text{Signal}_{\text{DQM}}^{(\text{i})}(t_5) &= \frac{1}{4} e^{-i(\phi_1 - \phi_2 + 2\phi_3 - 4\phi_4 + \phi_5)} e^{-2t_{\text{DQ}}^{(\text{DQM})}/T_2^D - t_5/(2/T_2^S + 1/T_1)} \\ &\times \text{Tr} \left[\left\{ P_{11}^3 M_1 P_{14}^2 \dagger P_{41}^3 \dagger + P_{14}^3 M_2 P_{44}^2 \dagger P_{44}^3 \dagger + (P_{12}^3 M_3 + P_{13}^3 M_4) \left(P_{24}^2 \dagger P_{42}^3 \dagger + P_{34}^2 \dagger P_{43}^3 \dagger \right) \right\} \right. \\ &\left. - \left\{ P_{11}^3 P_{11}^2 M_1 \dagger P_{41}^3 \dagger + P_{14}^3 P_{41}^2 M_2 \dagger P_{44}^3 \dagger + (P_{12}^3 P_{21}^2 + P_{13}^3 P_{31}^2) \left(M_3 \dagger P_{42}^3 \dagger + M_4 \dagger P_{43}^3 \dagger \right) \right\} \right]; \end{aligned} \quad (21)$$

$$\begin{aligned} \text{Signal}_{\text{DQM}}^{(\text{ii})}(t_5) &= -\frac{1}{4} e^{-i(\phi_1 - \phi_2 - 2\phi_3 + 4\phi_4 + 3\phi_5)} e^{-2t_{\text{DQ}}^{(\text{DQM})}/T_2^D - t_5/(2/T_2^S + 1/T_1)} \\ &\times \text{Tr} \left[\left\{ P_{41}^3 M_1 P_{14}^2 \dagger P_{11}^3 \dagger + P_{44}^3 M_2 P_{44}^2 \dagger P_{14}^3 \dagger + (P_{42}^3 M_3 + P_{43}^3 M_4) \left(P_{34}^2 \dagger P_{13}^3 \dagger + P_{24}^2 \dagger P_{12}^3 \dagger \right) \right\} \right. \\ &\left. - \left\{ P_{41}^3 P_{11}^2 M_1 \dagger P_{11}^3 \dagger + P_{44}^3 P_{41}^2 M_2 \dagger P_{14}^3 \dagger + (P_{42}^3 P_{21}^2 + P_{43}^3 P_{31}^2) \left(M_3 \dagger P_{12}^3 \dagger + M_4 \dagger P_{13}^3 \dagger \right) \right\} \right]. \end{aligned} \quad (22)$$

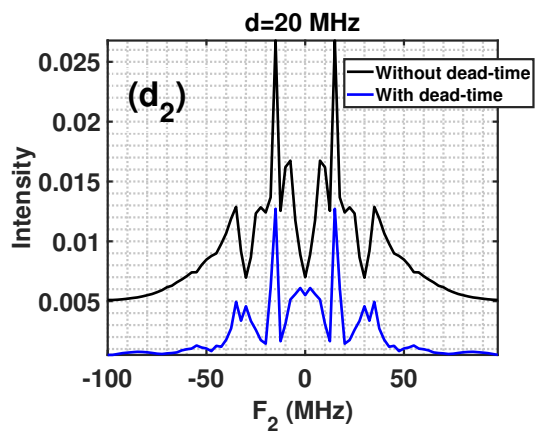
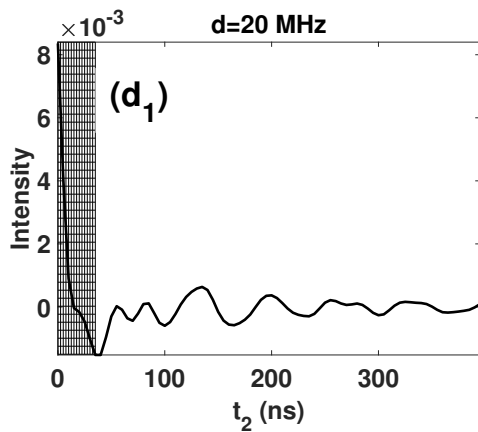
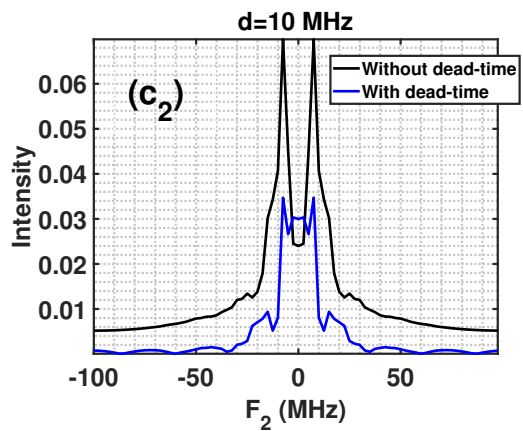
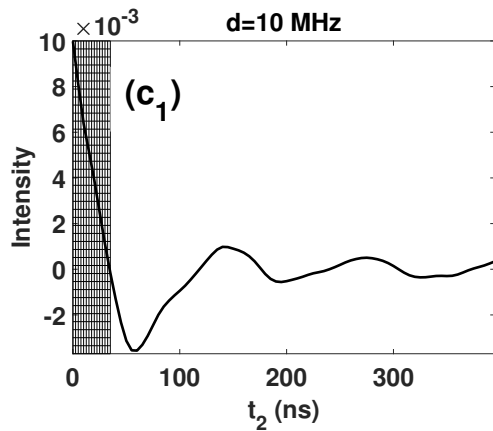
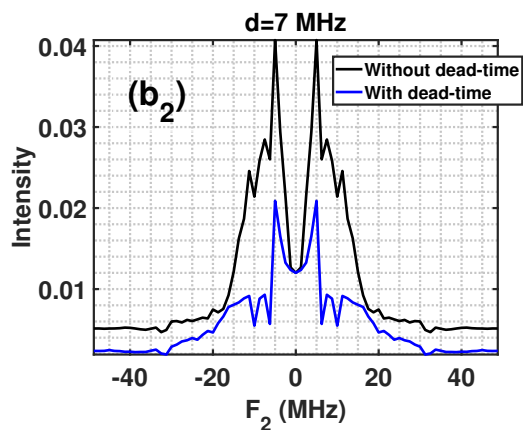
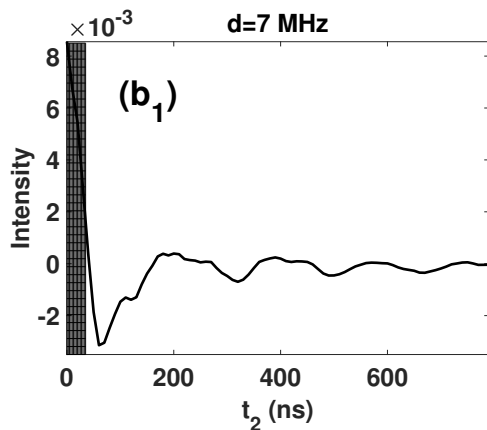
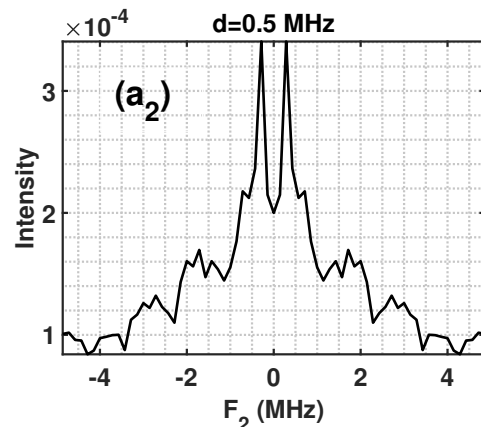
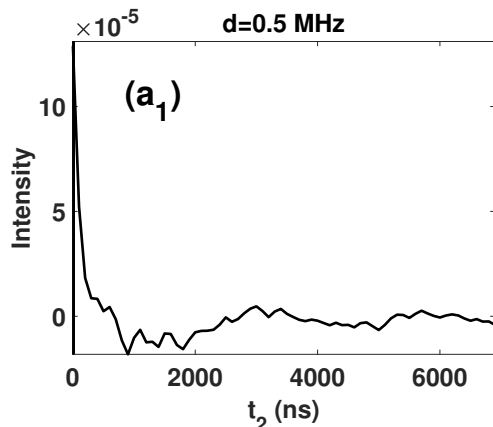
The M_i , $i = 1, 2, 3, 4$ terms in Eqs. (21) and (22) are defined in Appendix B below. The five-pulse DQM signal, is then:

$$\text{Signal}_{\text{DQM}}(t_5) = \text{Signal}_{\text{DQM}}^{(\text{i})}(t_5) + \text{Signal}_{\text{DQM}}^{(\text{ii})}(t_5). \quad (23)$$

It is seen from Eqs. (21) and (22) that the main dipolar peaks for a chosen orientation of the two nitroxide dipoles with respect to the dipolar axis, oriented at an angle θ with respect to the lab axis, occur at $\pm d \times (3 \cos^2 \theta - 1)$ in the Fourier transform taken with respect to time variable t_5 . This shows that the Pake doublet for the 1D five-pulse DQM signal, occurs at $\pm d$ in the Fourier transform of the signal, following the same discussion as that for DQ sequence at the end of Sec. 2.5.1.

3. Exact Numerical Simulation of Coherence Transfer

By using numerical techniques one can carry out the simulations rigorously without making any approximations. It is important to have an estimate of the coherence transfer, $T_{m \rightarrow n}$, which is the probability of transition from the pathway m to the pathway n , since the intensity of the signal increases with increasing coherence transfer. It is calculated as follows.



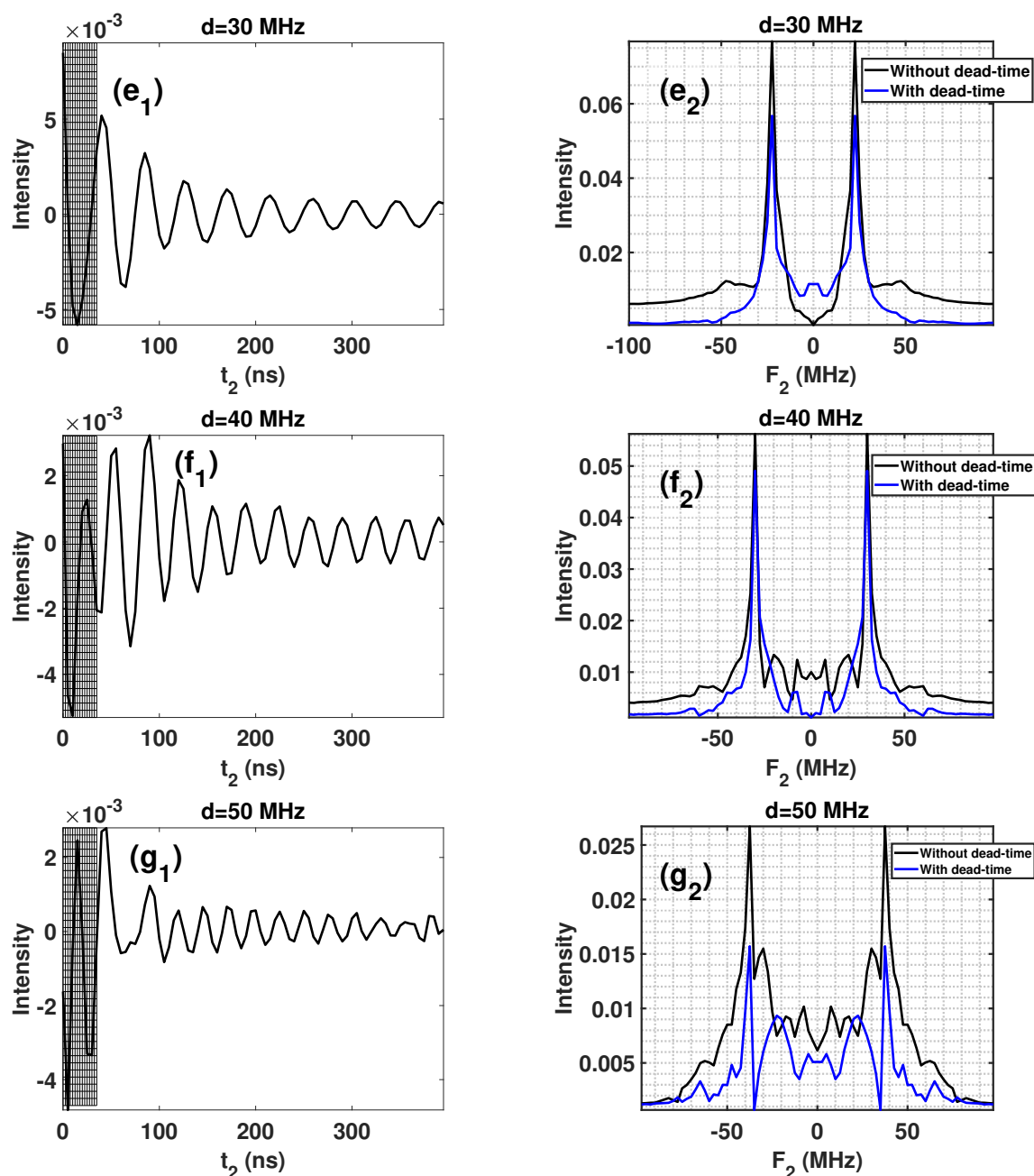
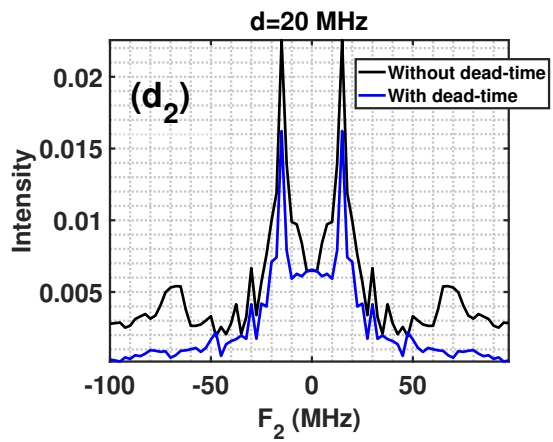
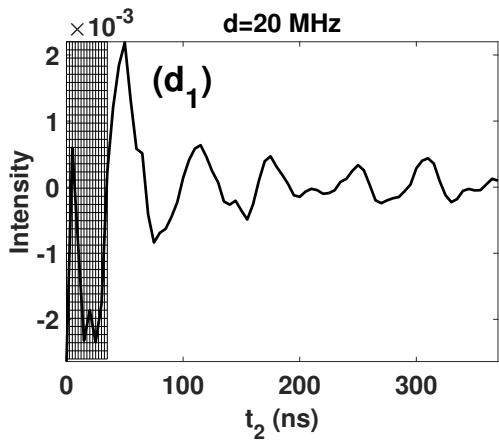
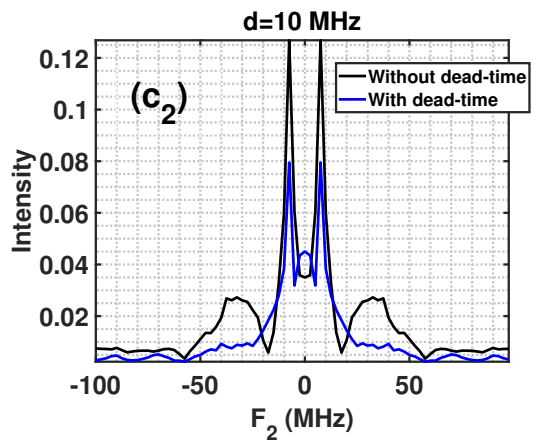
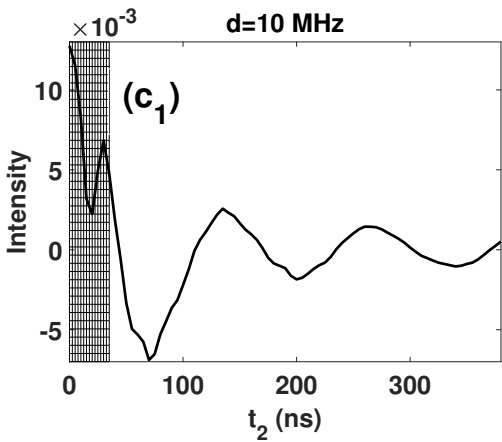
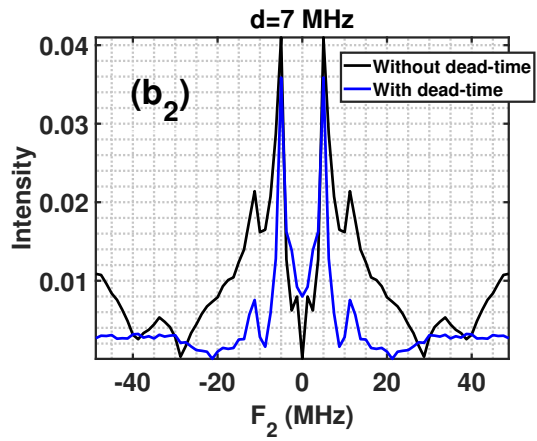
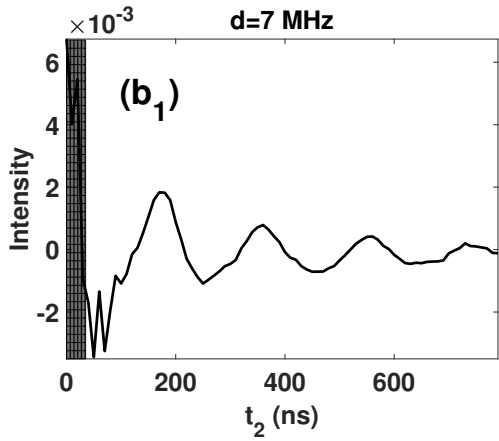
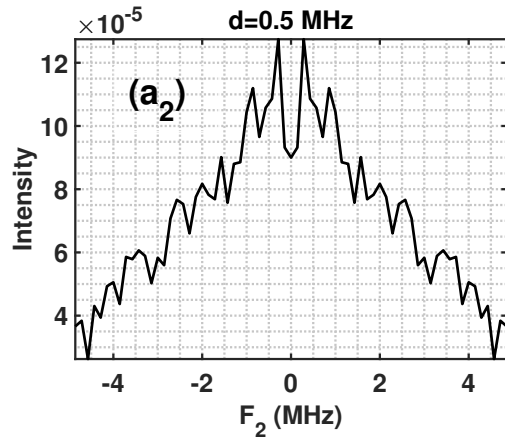
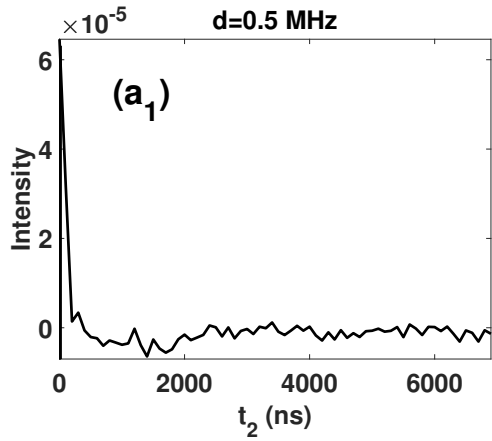


Figure 3. Dependence of the two-pulse DQ signal on the dipolar-coupling constant for a polycrystalline sample, averaged over twenty Monte-Carlo orientations of the nitroxide dipoles: left (a_1 , b_1 , c_1 , d_1 , e_1 , f_1 , g_1): time domain DQ signals for $t_2 = 2t_1$ and right (a_2 , b_2 , c_2 , d_2 , e_2 , f_2 , g_2): their Fourier transforms (Pake doublets) for $d = 0.5, 7.0, 10, 20, 30, 40, 50$ MHz. In all simulations, the amplitude of the irradiation microwave pulse B_1 is 10 G and the duration, t_p , for both pulses is 80 ns. All the other parameters used for the simulations are the same those listed in Table 1. The relaxation is not considered in these simulations. All Pake doublets appear at $\pm 3d/4$. The same dead time, $t_d = 35$ ns, as that reported in [3], is used here. The time-domain signal in the initial 35 ns interval, shown as hatched is lost in the dead-time of the pulse. The corresponding Fourier transform with respect to both t_2 and $t_2 - t_d$ are plotted, shown in black and blue, respectively.



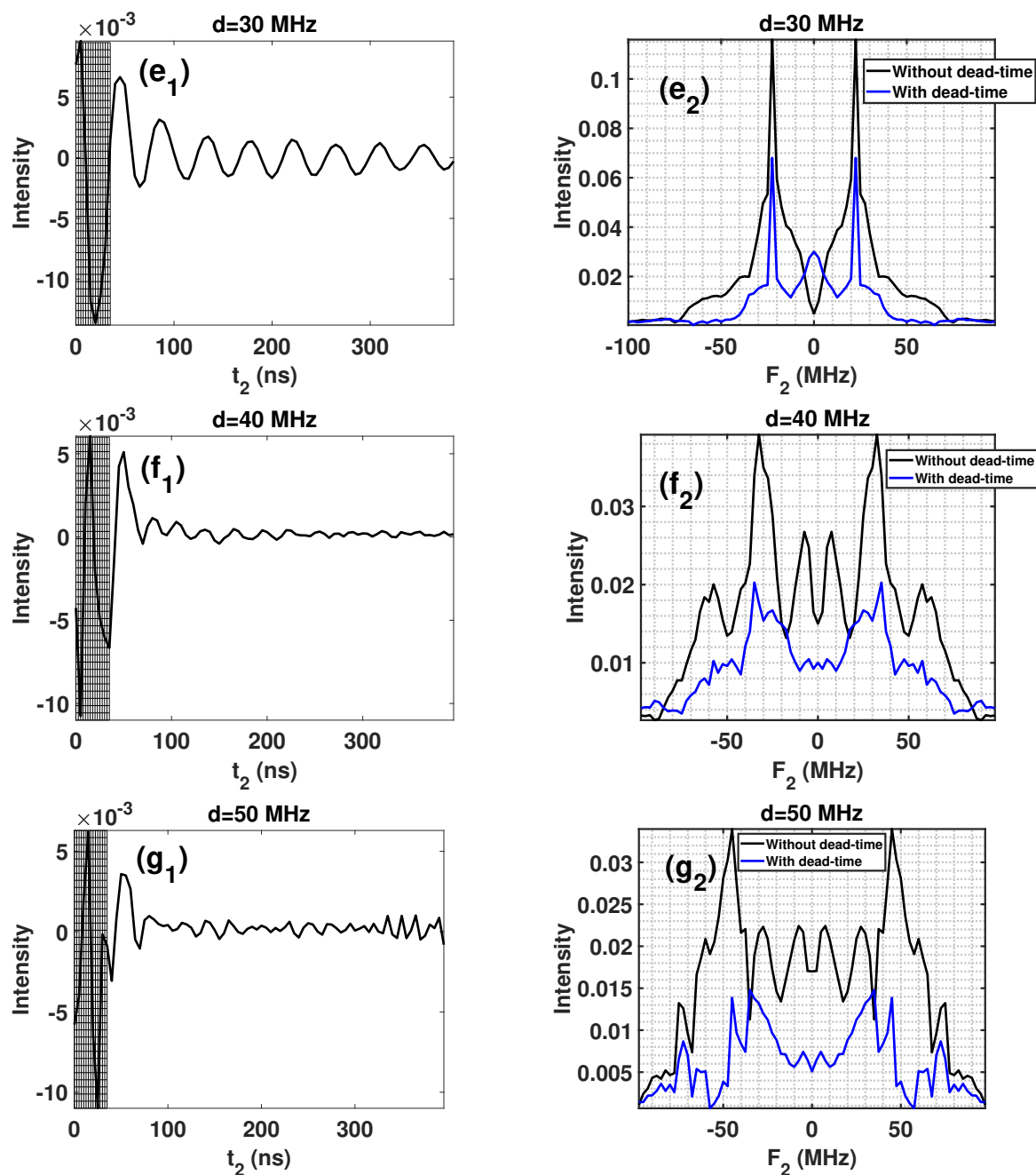


Figure 4. The same details as in the caption of Fig. 3, except here $B_1 = 60$ G and $t_p = 65$ ns, corresponding to the maximum coherence efficiencies for both $T_{0 \rightarrow 2}$ and $T_{2 \rightarrow -1}$ as discussed in Sec. 3.

3.1. Procedure for calculation

The density matrix for the pathway n after phase cycling subsequent to the application of a pulse is proportional to the spin operator corresponding to the coherence pathway n , which is S_z for the coherence pathway $p = 0$ (needed for five-pulse DQM only), S_{\pm} for the coherence pathways $p = \pm 1$ and $(S_{\pm} S_{\pm})$ for the coherence pathways $p = \pm 2$. The coherence transfer, $T_{m \rightarrow n}$, for the pathway n is then obtained by taking the trace of the density matrix resulting by the action of the pulse with the adjoint of the projection operator matrix for the coherence pathway n , listed in [14].

3.1.1. Efficiency of coherence transfer

The coherence-transfer efficiency for the transitions $0 \rightarrow 2$ and $2 \rightarrow -1$ in a DQ experiment is zero for a non-selective pulse [1]. With the application of a finite pulse, however, one can obtain non-zero coherence transfers $T_{0 \rightarrow 2}$ and $T_{2 \rightarrow -1}$. Using the rigorous numerical calculation, wherein one considers the full static spin Hamiltonian during the pulse, it is shown here that, indeed, $T_{0 \rightarrow 2}$ and $T_{2 \rightarrow -1}$ are non-zero for the system of coupled nitroxides as effected by a pulse of finite duration.

The results of numerical simulations for the coherence transfers $T_{0 \rightarrow 2}$ and $T_{2 \rightarrow -1}$ described above for a polycrystalline sample are plotted as functions of the amplitude of the irradiation microwave field B_1 and the duration of the pulse t_p in Figs. 8, 9, 10 for $d = 10, 20, 30$ MHz, respectively. It is seen by comparison that a maximum efficiency is found to occur for both $T_{0 \rightarrow 2}$ and $T_{2 \rightarrow -1}$, with an experimentally achievable $B_1 = 60$ G and $t_p = 65$ ns for all the three values of d considered here. These $T_{0 \rightarrow 2}$ and $T_{2 \rightarrow -1}$ values are about (0.03, 0.08, 0.11) and (0.03, 0.06, 0.10) for $d = 10, 20, 30$ MHz, respectively. The same values of $(B_1, t_p) = (60 \text{ G}, 65 \text{ ns})$ that correspond to these maxima are used for the calculation of the Pake doublets in the Fourier transform of the DQ signal in Figs. 4(a₂)–(g₂) and 5(a), (b).

4. Calculation of signal in the absence of relaxation

The best way to calculate pulsed EPR signals rigorously is by employing numerical techniques using the eigenvalues and eigenvectors of the Hamiltonian matrix. The details of the calculations presented in this section, based on the algorithm developed by Misra to calculate the six-pulse DQC signal [2], are quite general, applicable to both one- and two- dimensional two-pulse DQ and five-pulse DQM signals.

In the magnetic basis, the static Hamiltonian H_0 is not diagonal; the eigenvalues of H_0 are obtained by the diagonalization $U^\dagger H_0 U = E$, where E is the eigenvalue matrix, whose diagonal elements are the eigenvalues, whereas the columns of matrix U are the corresponding eigenvectors.

To calculate the k -pulse signal, one starts with the initial density matrix, which is S_Z as discussed in Sec. 2.2, in the direct-product space: $\rho_0 \rightarrow S_Z = \frac{\sigma_{z_1}}{2} \otimes \mathbb{1}_{S_2} \otimes \mathbb{1}_{I_1} \otimes \mathbb{1}_{I_2} + \mathbb{1}_{S_1} \otimes \frac{\sigma_{z_2}}{2} \otimes \mathbb{1}_{I_1} \otimes \mathbb{1}_{I_2}$, where σ_{z_i} ; $i = 1, 2$ are the Pauli spin matrices for the electron spin. The final density matrix $\rho_f(\mathbf{t}_k)$ with $k = 2, 5$ for two- and five-pulse signals, respectively, is obtained by successive applications of the k pulses to it using Eq. (15), followed by free evolution over the coherence pathways, as shown in Fig. 2 for each pulse sequence, using Eqs. (13) and (14) without the exponential factor that considers the effect of relaxation. The complex signal is then obtained using Eq. (16). The polycrystalline average and Pake doublets are calculated using Eqs. (17) and (18), respectively. Thereafter, the relevant Gaussian inhomogeneous broadening factor is multiplied to Eq. (18) for Pake doublets, as discussed in Sec. 2.4. The flow chart for numerical simulations is given in Appendix A.

5. Orientational selectivity in two-pulse DQ and five-pulse DQM signals

There occurs orientational selectivity when the signal is determined predominantly by those biradicals, whose dipolar axes are oriented in a narrow range about the static magnetic field direction. This is further discussed in detail in the following two sections involving numerical calculation and analytical treatment of orientational selectivity.

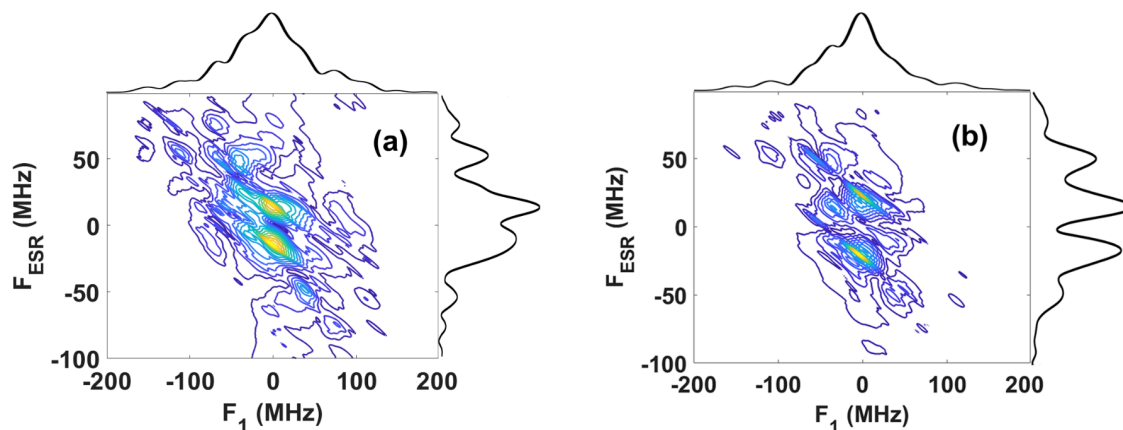


Figure 5. The two-dimensional top views of the Fourier transforms of the DQ signal as a function of the double quantum frequency, denoted as F_1 , corresponding to the time t_1 in Fig. 2(a), showing the pulse sequence, and the ESR frequency, F_{ESR} , corresponding to the time t_2 after the second pulse as shown in Fig. 2(a) for a coupled nitroxides biradical with the coupling constants: (a) $d = 20$ MHz and (b) $d = 30$ MHz. The corresponding 1D spectra, are joined on the top and on the right-hand sides of the top views, as obtained by the summation along the F_{ESR} and F_1 axes, respectively, and by dividing by the number of data points to calculate averages. The attached figures on the right-hand sides represent the CW ESR spectra, wherein the static field is kept at the fixed value 3323 G and the frequency is varied. The amplitude of the radiation microwave field $B_1 = 60$ G, a pulse of sufficient intensity to excite most of the spins in the sample, and the duration of the pulse $t_p = 65$ ns is used for both pulses, corresponding to the maximum coherence efficiencies for both $T_{0 \rightarrow 2}$ and $T_{2 \rightarrow -1}$ are used for the simulations. All other parameters used for the simulations are the same as those listed in Table 1. The relaxation is not considered here.

5.1. Exact numerical calculation

For these calculations, it is first noted that the forbidden transition $p = 0 \rightarrow 2$ in the two-pulse DQ and five-pulse DQM sequences becomes possible only in the presence of the dipolar interaction and a for a finite pulse as discussed in Sec. 5.2 below. When this condition is satisfied, the coherence transfer $T_{0 \rightarrow 2}$ is found to be much larger in a very narrow range about four specific values of θ , the angle between the dipolar axis and the external magnetic field. These specific four angles depend on the amplitude of the irradiation field, B_1 , and the dipolar interaction, d , as the simulations presented here show for $T_{0 \rightarrow 2}$ for three values of $d = 20, 30, 40$ and 40 MHz as displayed in Figs. 6(a), 6(b), 6(c), 6(d), respectively, for varying values of B_1 . It is found from these figures that for smaller B_1 there are, indeed, two such values of θ in the range $0^\circ \leq \theta_0 \leq 90^\circ$, and two more about its supplementary angle 125.26° , for which the $T_{0 \rightarrow 2}$ value is much larger than those for other values of θ . These values are found to be situated symmetrically within 10° away from the magic angle 54.74° at which $(3 \cos^2 \theta - 1) = 0$, and its supplementary angle 125.26° , becoming closer to the magic angle as d increases, as seen from Fig. 6, giving rise to orientational selectivity; implying that these spins will be preferentially pumped from $p = 0$ to $p = 2$ coherence state. This implies that there occurs *orientational selectivity*. This is a first-ever novel result, as far as orientational sensitivity is concerned, found with the help of extensive quantitative simulations for the first time. This orientational selectivity of the forbidden DQ signal occurs up to a maximum value of B_1 that depends on d . These maximum B_1 values are 1.5, 2.0, 3.0, and 4.0 G for $d = 20, 30, 40$ and 50 MHz, respectively, for both, the two-pulse DQ and five-pulse DQM sequences.

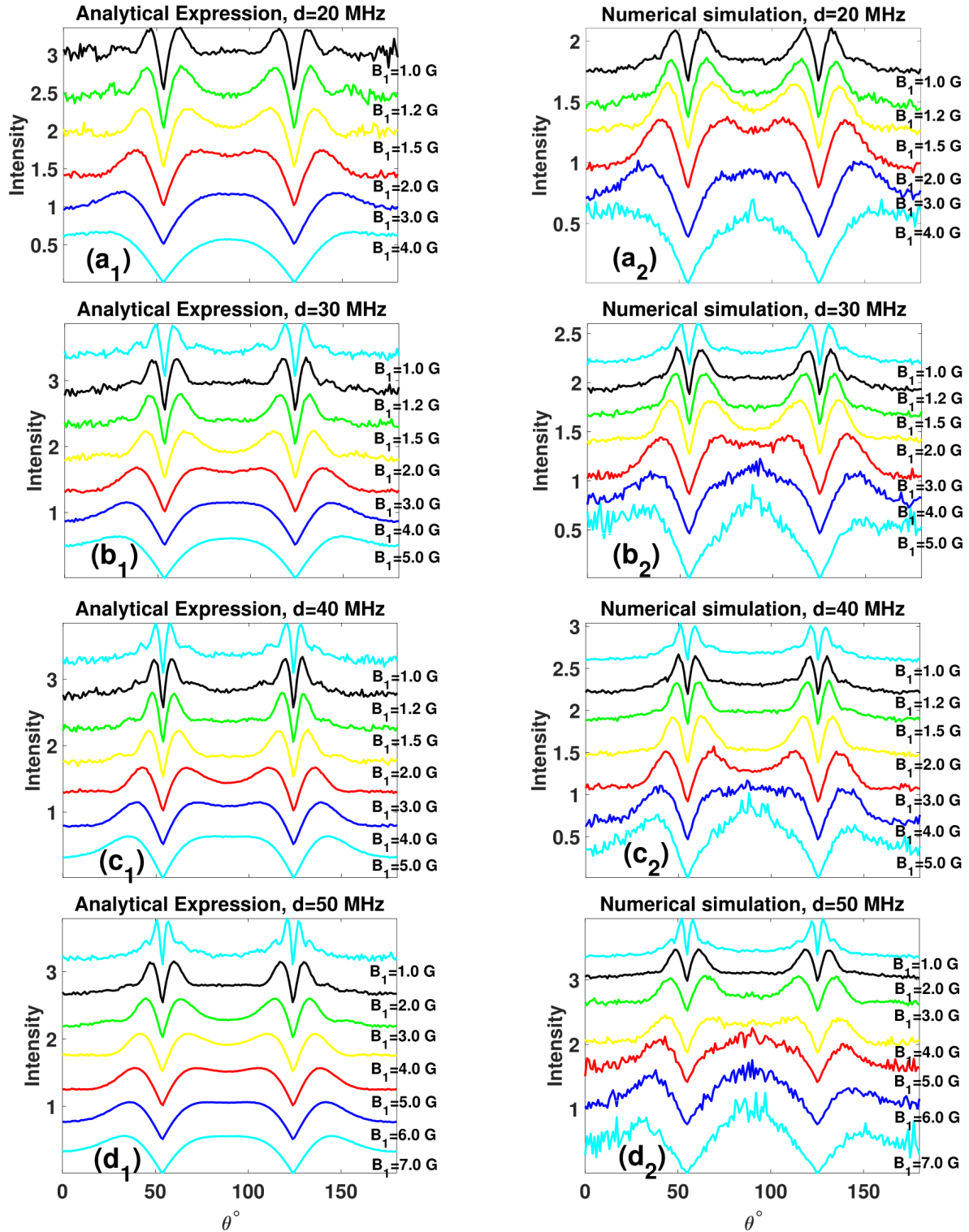


Figure 6. The coherence transfer $T_{0 \rightarrow 2}$ plotted as function of θ , as calculated: left (a₁, b₁, c₁, d₁) using the analytical expression, Eq. (31), and right (a₂, b₂, c₂, d₂) rigorously using numerical simulations for different values of the amplitude of the irradiation microwave pulse, B_1 , indicated next to each plot for (a₁, a₂) $d = 20$ MHz, (b₁, b₂) $d = 30$ MHz, (c₁, c₂) $d = 40$ MHz and (d₁, d₂) $d = 50$ MHz. The duration of the pulse t_p in each case is chosen consistent with a nominal $\pi/2$ pulse and amplitude B_1 . The two sets, calculated using analytical expressions and exact numerical algorithm, are found to be in very good agreement with each other.

In order to display orientational selectivity, the coherence transfer efficiency $T_{0 \rightarrow 2}$ is plotted as a function of θ , the angle between the dipolar axis and the external magnetic field, as calculated using the analytical expression (31), in Figs. 6 (a₁), (b₁), (c₁) and (d₁) for $d = 20, 30, 40, 50$ MHz, respectively, for several weak irradiation microwave fields $B_1 (\leq 5.0G)$, each for an appropriate time interval t_p , so that the tip angle $\beta = \pi/2$. In each case, a polycrystalline average is taken over 20 simulations, carried out with randomly generated set of the five independent orientation angles for the two nitroxide dipoles, using the Monte-Carlo technique. For comparison, the same simulations are carried out numerically without neglecting any terms in the spin Hamiltonian. The results are plotted in Figs. 6 (a₂), (b₂), (c₂), (d₂), alongside the ones obtained using the analytical expressions. The two sets are found to be in very good agreement with each other, justifying the validity of the analytical expressions (31) and (32).

5.2. Analytical treatment of orientational selectivity

It is useful to have analytical expressions for a quick calculation and evaluation of important features of coherence transfer, i.e., orientational selectivity. To this end, some approximations are made to simplify the calculation. One of the approximations made in the following treatment is to neglect the Zeeman and hyperfine terms with coefficients (C_1, C_2) and (A_1, B_1, A_2, B_2) , respectively, in the spin Hamiltonian given by Eq. (1). However, one has to compensate for it by modifying the frequency ω_1 to an effective frequency, $\omega_{1\text{eff}}$, as discussed below.

Effective frequency of rotation, $\omega_1(\omega_{1\text{eff}})$. The presence of the pulse, i.e., the microwave field, B_1 , tips the magnetization differently out of the precession about the z-axis, where it was before the application of the pulse. This implies that the magnetization is now tipped by an effective magnetic field \mathbf{B}_{eff} , which is the vector sum of \mathbf{B}_1 and \mathbf{B}_0 , causing the magnetizations of the two electrons to tip around their respective $\mathbf{B}_{\text{eff}} = \mathbf{B}_1 + \mathbf{B}_0$, at a faster effective rate [35]. This is considered for the two dipoles of the biradical by taking the average of the effective angular velocities for the two dipoles, since only one dipole is flipped by the pulse at a time:

$$\omega_{1\text{eff}} = \gamma_e B_{1\text{eff}} = (\omega_1^2 + C_1^2)^{1/2} + (\omega_1^2 + C_2^2)^{1/2}/2, \quad (24)$$

where $\omega_1 = \gamma_e B_1$ and C_1, C_2 , respectively, are the coefficients of S_{z_1} and S_{z_2} in the spin Hamiltonian, Eq. (2), given by Eq. (A.4) in [14]. From Eq. (24), it is seen that for a strong pulse, i.e., $\omega_1 \gg C_1, C_2$, one can approximate $\omega_{1\text{eff}}$ by ω_1 , whereas for weak pulse, the effect of Zeeman terms must be included. The Zeeman and hyperfine terms in the static Hamiltonian, given by Eq. (1), are responsible for a detuning from the carrier frequency as discussed above in this section. As a result, ω_1 will be substituted here by $\omega_{1\text{eff}}$, which is given by Eq. (24), following the discussion given by Raitisimiring and Borbat [35]. Then only the dipolar-interaction term H_{12} need to be taken into consideration for the calculation of coherence transfer, which makes it simpler to derive analytical expressions, as follows.

In the magnetic basis of the two electrons, the matrix for H_0 in the direct-product space (see Appendix B in [14]), is then given as

$$H_{12} = \frac{a}{3}(2S_z^2 - S_x^2 - S_y^2) = \frac{a}{3} \begin{pmatrix} 1 & 0 & 0 & 0 \\ 0 & -1 & -1 & 0 \\ 0 & -1 & -1 & 0 \\ 0 & 0 & 0 & 1 \end{pmatrix}, \quad (25)$$

where $S_z = S_{z_1} \otimes \mathbb{1}_{S_2} + \mathbb{1}_{S_1} \otimes S_{z_2}$, $S_x = S_{x_1} \otimes \mathbb{1}_{S_2} + \mathbb{1}_{S_1} \otimes S_{x_2}$, $S_y = S_{y_1} \otimes \mathbb{1}_{S_2} + \mathbb{1}_{S_1} \otimes S_{y_2}$, and

$a = \frac{3d}{4}(3\cos^2\theta - 1)$. The matrix for H_p , using $\omega_{1\text{eff}}$, is:

$$H_p = \frac{1}{2}\omega_{1\text{eff}} \begin{pmatrix} 0 & e^{-i\phi} & e^{-i\phi} & 0 \\ e^{i\phi} & 0 & 0 & e^{-i\phi} \\ e^{i\phi} & 0 & 0 & e^{-i\phi} \\ 0 & e^{i\phi} & e^{i\phi} & 0 \end{pmatrix}. \quad (26)$$

For the calculation of the coherence transfer, the phase of the pulse, ϕ , is set equal to zero. The eigenvalues, E_p and the eigenvectors, U , of matrix $H_{12} + H_p$, using Eqs. (25) and (26), are given as

$$E_p = U^\dagger (H_{12} + H_p) U = \begin{pmatrix} 0 & 0 & 0 & 0 \\ 0 & a/3 & 0 & 0 \\ 0 & 0 & -\frac{1}{6}(3\Omega + a) & 0 \\ 0 & 0 & 0 & \frac{1}{6}(3\Omega - a) \end{pmatrix}, \quad (27)$$

where

$$U = \begin{pmatrix} 0 & -\frac{1}{\sqrt{2}} & \frac{\sqrt{2}\omega_{1\text{eff}}}{\sqrt{(a+\Omega)^2+4\omega_{1\text{eff}}^2}} & \frac{\sqrt{2}\omega_{1\text{eff}}}{\sqrt{(a-\Omega)^2+4\omega_{1\text{eff}}^2}} \\ -\frac{1}{\sqrt{2}} & 0 & -\frac{\Omega+a}{\sqrt{2}\sqrt{(a+\Omega)^2+4\omega_{1\text{eff}}^2}} & \frac{\Omega-a}{\sqrt{2}\sqrt{(a-\Omega)^2+4\omega_{1\text{eff}}^2}} \\ \frac{1}{\sqrt{2}} & 0 & -\frac{\Omega+a}{\sqrt{2}\sqrt{(a+\Omega)^2+4\omega_{1\text{eff}}^2}} & \frac{\Omega-a}{\sqrt{2}\sqrt{(a-\Omega)^2+4\omega_{1\text{eff}}^2}} \\ 0 & \frac{1}{\sqrt{2}} & \frac{\sqrt{2}\omega_{1\text{eff}}}{\sqrt{(a+\Omega)^2+4\omega_{1\text{eff}}^2}} & \frac{\sqrt{2}\omega_{1\text{eff}}}{\sqrt{(a-\Omega)^2+4\omega_{1\text{eff}}^2}} \end{pmatrix}, \quad (28)$$

and

$$\Omega = \sqrt{a^2 + 4\omega_{1\text{eff}}^2}. \quad (29)$$

Then the pulse propagator, including the dipolar Hamiltonian, is expressed as

$$e^{-i(H_{12}+H_p)t_p} = U e^{-iE_p t_p} U^\dagger. \quad (30)$$

Following the procedure to calculate the coherence transfer as described in Sec. 3.1 above and using the pulse propagator, given by Eq. (30), the coherence transfer for the transition $0 \rightarrow 2$ is:

$$\begin{aligned} T_{0 \rightarrow 2} &= \text{Abs} \left\{ \text{Tr} \left[(S_- S_-) / 2 e^{-i(H_{12}+H_p)t_p} S_z e^{i(H_{12}+H_p)t_p} \right] \right\} \\ &= \text{Abs} \left[\frac{a \cos(at_p/2) \sin(\Omega t_p/2)}{\Omega} - \sin(at_p/2) \cos(\Omega t_p/2) \right]. \end{aligned} \quad (31)$$

In the middle part of Eq. (31), a division of 2 has been added after the first equality to extract the (1, 4) element of the transformed density matrix. Likewise, for the transition $2 \rightarrow -1$, the magnitude of the coherence transfer is:

$$\begin{aligned} T_{2 \rightarrow -1} &= \text{Abs} \left\{ \text{Tr} \left[S_+ e^{-i(H_{12}+H_p)t_p} (S_+ S_+) / 2 e^{i(H_{12}+H_p)t_p} \right] \right\} \\ &= \text{Abs} \left[\frac{2\omega_{1\text{eff}} \sin(\Omega t_p/2) (a \sin(\Omega t_p/2) - \Omega \sin(at_p/2))}{\Omega^2} \right]. \end{aligned} \quad (32)$$

After the first equality in Eqs. (32), a division of 2 has been added to render the (1, 4) element of the density matrix corresponding to $p = +2$ state equal to unity. It is noted from Eqs. (31) and (32) that in the limit when the dipolar coupling, d , or the duration of the pulse, t_p approach zero, both the coherence transfers $T_{0 \rightarrow 2}$ and $T_{2 \rightarrow -1}$ vanish. *This implies that one needs a finite pulse, together with the dipolar interaction, to produce a non-zero coherence transfer.*

6. Signal due to spin relaxation in a polycrystalline sample

In Sec. 4., the signal for a polycrystalline sample is calculated in the absence of relaxation. To consider the effect of the relaxation for a powder average, the stretched exponential approach is used here, following the discussion in [29, 30], which considers the average effect of different relaxation times for different orientations of the dipolar axis with respect to the magnetic field by a single exponential with the exponent β . For the present cases this is discussed as follows.

Averaging over relaxation times T_1 , T_2^S and T_2^D . According to Eqs. (13) and (14), after time t , for a single-orientation of the dipolar axis with respect to the external magnetic field, the effect of relaxation on the signal is considered by multiplying the calculated signal by the exponential factors $\exp(-t/T_2^S)$, $\exp(-t/T_2^D)$ and $\exp(-t/T_1)$ for the coherence pathways $p = \pm 1$, $p = \pm 2$ and $p = 0$, respectively, with the time constants T_2^S , T_2^D , T_1 , appropriate for that orientation. Then the cumulative effect of the relaxation on the multi-pulse signals, considering all coherence pathways as shown in Fig. 2, is calculated by multiplying the signal with two and five decaying exponential functions for two- and five-pulse sequences, respectively. For a polycrystalline sample, the signal is averaged over different values of (θ, ϕ) , each characterized by different relaxation times $T_1(\eta, \lambda_1, \lambda_2)$, $T_2^S(\eta, \lambda_1, \lambda_2)$, $T_2^D(\eta, \lambda_1, \lambda_2)$. The effect of relaxation at the top of the echo, i.e., at $t_2 = 2t_1$ for two-pulse DQ and at $t_5 = t_1$ for five-pulse DQM, is then expressed as

$$S_{0\text{avg}}^{\text{DQ}}(\mathbf{t}_k) = \sum_{\eta, \lambda_1, \lambda_2} S_0(\mathbf{t}_k, \eta, \lambda_1, \lambda_2) \exp(-t_1(1/T_2^D(\eta, \lambda_1, \lambda_2) + 2/T_2^S(\eta, \lambda_1, \lambda_2))); \quad (33)$$

$$S_{0\text{avg}}^{\text{DQM}}(\mathbf{t}_k) = \sum_{\eta, \lambda_1, \lambda_2} S_0(\mathbf{t}_k, \eta, \lambda_1, \lambda_2) \times \exp \left[-2t_{\text{DQ}}^{(\text{DQM})}/T_2^D(\eta, \lambda_1, \lambda_2) - t_1(2/T_2^S(\eta, \lambda_1, \lambda_2) + 1/T_1(\eta, \lambda_1, \lambda_2)) \right], \quad (34)$$

where $S_0(\mathbf{t}_k, \eta, \lambda_1, \lambda_2)$ is the EPR signal calculated without relaxation as given by Eq. (16). Assuming the same orientational distribution function for the three relaxation times $T_1(\eta, \lambda_1, \lambda_2)$, $T_2^S(\eta, \lambda_1, \lambda_2)$ and $T_2^D(\eta, \lambda_1, \lambda_2)$ over $(\eta, \lambda_1, \lambda_2)$, Eq.(33), becomes modified, in the stretched exponential approach, as follows [29, 30]:

$$S_{0\text{avg}}^{\text{DQ}}(\mathbf{t}_k) = S_{0\text{avg}}(\mathbf{t}_k) \exp \left(- [t_1(1/T_{2\text{str}}^D + 2/T_{2\text{str}}^S)]^\beta \right), \quad (35)$$

$$S_{0\text{avg}}^{\text{DQM}}(\mathbf{t}_k) = S_{0\text{avg}}(\mathbf{t}_k) \exp \left(- \left[2t_{\text{DQ}}^{(\text{DQM})}/T_{2\text{str}}^D + t_1(2/T_{2\text{str}}^S + 1/T_{1\text{str}}) \right]^\beta \right) \quad (36)$$

where, $S_{0\text{avg}}(\mathbf{t}_k)$ is the average of $S_0(\mathbf{t}_k, \eta, \lambda_1, \lambda_2)$ over all orientations $(\eta, \lambda_1, \lambda_2)$ as described by Eqs (17) and (18) for both DQ and DQM signals, and $T_{1\text{str}}$, $T_{2\text{str}}^S$ and $T_{2\text{str}}^D$ are the ‘‘stretched’’ relaxation times over zero ($p = 0$), single ($p = 1$ pathway) and double ($p = 2$ pathway) quantum states, respectively. The stretching parameter, β , which is related to the distribution function of the relaxation times in Eqs. (35) and (36), ranges between zero and one [29, 30]. Equations (35) and (36) reduce to the system with orientation-independent relaxation times in the limit when $\beta \rightarrow 1$. It is noted that, in general, there are two different stretching parameters, $\beta^{(S)}$ and $\beta^{(D)}$, characterizing the orientational distribution of the single and double quantum relaxation times which are to be found by fitting the simulation to the experimental data [29, 30]. In this paper, since the experimental values for $\beta^{(S)}$ and $\beta^{(D)}$ are not available, and $\beta^{(D)}$ affects only the intensity of the signal, the value $\beta^{(S)} = \beta^{(D)} = \beta = 0.8$ is used, being the average of the two values 0.78 and 0.85, derived in [29, 30].

7. Effect of dead-time on two-pulse DQ and five-pulse DQM signals

Immediately after a pulse, recording the signal is not possible due to the so-called dead-time, denoted as t_d hereafter, of the spectrometer. The best value of t_d as reported in [3] is 35 ns at X-band. This value will be used here to not consider the initial signal up to the dead-time, in the calculation following the procedure given in Sec. 4; shorter values of dead-time are possible today with the use of more powerful klystrons.

Due to a significant initial part of the signal is lost during the dead-time, t_d , the modulation depth can only be measured for $d = 0.5$ MHz, as seen from Figs. 3, 4, 11. However, the Pake doublets as a function of the reduced echo times $(t_2 - t_d)$ or $(t_5 - t_d)$ for DQ or DQM sequences, respectively, are still found undistorted and centered at $\pm 3d/4$ and $\pm d$, for two-pulse DQ and five-pulse DQM, respectively, albeit slightly narrowed and reduced in intensities, as seen from Figs. 3, 4, 11. Thus, the Fourier transforms with respect to the reduced echo times also provide a measure of the dipolar constant, which, in turn, enables one to calculate the distance between the two nitroxides.

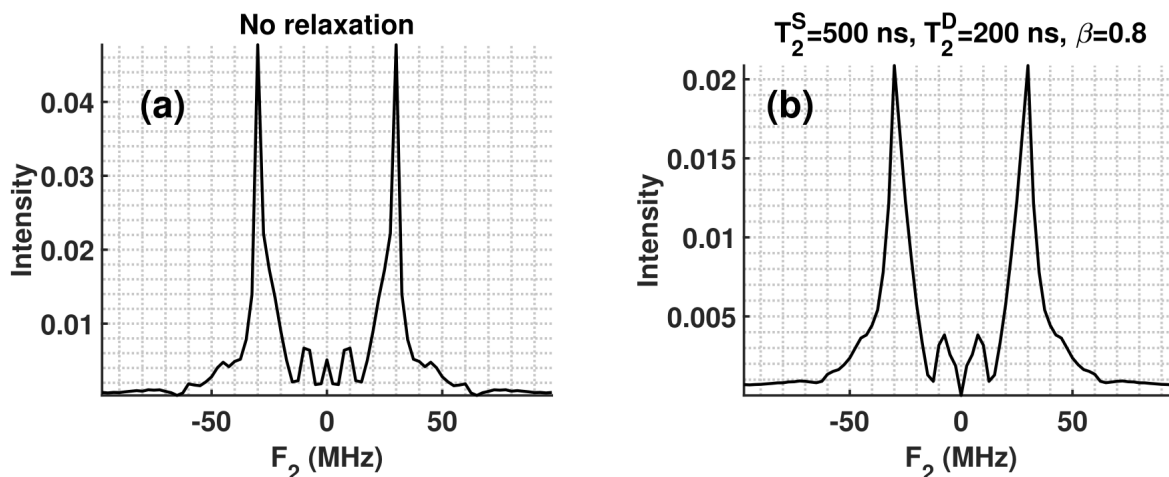


Figure 7. The effect of relaxation on the DQ signal for a polycrystalline sample, averaged over twenty Monte-Carlo orientations of the nitroxide dipoles. The Fourier transform as a function of t_1 of the time domain DQ signal at $t_2 = 2t_1$ for: (a) without taking relaxation into account and (b) with relaxation included for $T_2^S = 500$ ns and $T_2^D = 200$ ns using the stretching parameter $\beta = 0.8$ as discussed in Sec. 6. The dipolar coupling constant $d = 40$ MHz and the amplitude of the irradiation microwave pulse $B_1 = 10.0$ G are used in these simulations. The values of all the other parameters used in the simulations are the same as those listed in Table 1. Due to relaxation, the peaks are broadened in Fig. 7(b), and the intensity of the calculated Fourier transform of the DQ signal is reduced by about a factor of two.

The time-domain signals calculated with and without dead-time are shown in Figs. 3, 4, 11. The dead-time effect is shown by hatching the initial time interval t_d of the signal. The Fourier transforms of the two-pulse DQ and five-pulse DQM signals taken with respect to both echo-time and reduced echo-time variables are plotted, which show that the intensity of the Fourier transforms are reduced by including the dead-time. However, the Pake doublets still occur at $\pm 3d/4$ and $\pm d$, for two-pulse DQ and five-pulse DQM, respectively, although diminished in their intensities and widths.

7.1. Modulation depths of the calculated signals

The time dependent signal at the top of the echo due to the dipolar modulation in two-pulse DQ and five-pulse DQM signals for a given orientation $\eta = (\theta, \phi)$ of the external magnetic field with respect to the dipolar axis connecting the two nitroxides, and the five independent Euler angles $\lambda_1 = (\alpha_1 = 0, \beta_1, \gamma_1)$, $\lambda_2 = (\alpha_2, \beta_2, \gamma_2)$ can be written as [36,37]

$$V(t, \eta, \lambda_1, \lambda_2) = V_0[1 - \lambda(\eta, \lambda_1, \lambda_2)(1 - \cos(\omega(\theta)t))], \quad (37)$$

where V_0 is the amplitude of the signal at time $t = 0$; $\lambda(\eta, \lambda_1, \lambda_2)$ is the depth of the dipolar modulation at the orientation $(\eta, \lambda_1, \lambda_2)$ and

$$\omega(\theta) = d(3 \cos^2 \theta - 1). \quad (38)$$

For a polycrystalline sample, as described in Sec. 2, the signal is then:

$$V(t) = 4 \sum_{\lambda_1, \lambda_2} \int_0^\pi d\phi \int_0^{\pi/2} V_0[1 - \lambda(\eta, \lambda_1, \lambda_2)(1 - \cos(\omega(\theta)t))] \sin \theta d\theta. \quad (39)$$

The resulting time-domain signal has its maximum $V_{0\text{avg}}$ at time $t = 0$, and it oscillates around the equilibrium value V_{eq} . As a percentage, the depth of the modulation for a polycrystalline sample, Δ is:

$$\Delta(\%) = (V_{0\text{avg}} - V_{\text{eq}})/V_{0\text{avg}} \times 100. \quad (40)$$

Table 1. The values of the parameters used in the simulations of the pulsed-EPR DQ and DQM signals of the coupled nitroxide biradical.

Parameter	Value
Static magnetic field (B_0)	3323 G
Microwave frequency	9.266 GHz
Exchange constant (J)	0 MHz
Double quantum time $t_3 = t_4 = t_{\text{DQ}}^{\text{DQM}}$	50 ns
Stretched exponential parameter (β)	0.8
g -matrix $\tilde{\mathbf{g}} = (g_{xx}, g_{yy}, g_{zz})$	(2.0086, 2.0066, 2.0032)
Hyperfine matrix $\tilde{\mathbf{A}} = (A_{xx}, A_{yy}, A_{zz})$	(6.0 G, 6.0 G, 35.0 G)
Spin-lattice relaxation time (T_1)	10 μs

8. Discussion of results of numerical simulations

For reference, the values and definitions of the constants used in the numerical simulations are listed in Table 1 below. Following [1, 2] the exchange parameter J is set to zero in all the simulations in the present work. The simulations for the polycrystalline sample were carried out over a $90 \times 90 \{\cos \theta, \phi\}$ grid on the unit sphere for 20 different sets of five Euler angles $\{(0, \beta_1, \gamma_1), (\alpha_2, \beta_2, \gamma_2)\}$ with Monte-Carlo averaging to calculate the Pake doublets. In the

numerical simulations for distance measurement carried out here, only one variable time is used to calculate 1D (one-dimensional) signals, specifically for $t_2 = 2t_1$ for two-pulse DQ and $t_5 = t_1$ for five-pulse DQM signals. This results in a considerable saving of time in experimental measurements. As well, the simulations for a polycrystalline sample can be carried out using a much larger grid over the unit sphere because only a single time variable is needed. The results for the DQ and DQM sequences are described in Secs. 8.1 and 8.2 below.

8.1. Two-pulse DQ signal

The main features of the simulation for the coherence transfer for the DQ signal at X-band are as follows.

- (i) Figures 3 and 4 display the dependence of the 1D time-domain DQ signals for the dipolar-coupling constants: $d = 0.5, 7, 10, 20, 30, 40, 50$ MHz, simulated at the top of the echo i.e., at $t_2 = 2t_1$, along with their Fourier transforms as a function of t_2 . In Fig. 3, the amplitude of the radiation microwave field $B_1 = 10$ G and the duration of the finite pulses $t_p = 80$ ns and in Fig. 4, $B_1 = 60$ G and $t_p = 65$ ns, corresponding to the maximum coherence efficiency as discussed in Sec. 3, are used. The dead time of $t_d = 35$ ns, as that reported experimentally in [3], is assumed here. This means that the signal during the initial 35 ns, shown as hatched in Figs. 3 and 4, cannot be recorded in the experiment. To consider the effect on the Fourier transform of the signal that can be recorded, the Fourier transforms with respect to both t_2 and $t_2 - t_d$ are plotted in Figs. 3 and 4, shown in black and blue, respectively. It is seen that the Fourier transform taken with respect to $t_2 - t_d$ does not distort the Pake doublets, or its position. It reduces only the intensity and the width of the Fourier transform. For $d = 0.5$ MHz, the dead-time covers only a negligible part of the signal. The modulation depth, Δ , can then be calculated for this case. It is found to be almost 100%, as seen from Figs. 3 and 4. As for $d > 7$ MHz, Δ cannot be measured, because a significant part of the initial signal is lost in the dead-time. The Pake doublets in the Fourier transform of the DQ signals shown in Figs. 3 and 4, indeed, appear at $\pm 3d/4$ as deduced theoretically in Sec. 2.5.1.
- (ii) The top view plots of the two-dimensional Fourier transform of DQ signal for a coupled nitroxides biradical with the coupling constants: (a) $d = 20$ MHz and (b) $d = 30$ MHz, are shown in Fig. 5. The 2D Fourier transform is plotted as a function of the double quantum frequency, F_1 and F_{ESR} , the ESR frequency which are the Fourier variables corresponding to t_1 and t_2 in the DQ sequence, respectively. The corresponding 1D spectra, joined on the top and on the right-hand side of the contour plots, respectively, are obtained by integration along the ESR frequency and F_1 axes, and dividing by the number of data points to calculate averages. The joined figures on the right-hand side represent the CW ESR spectra. The amplitude of the radiation microwave field $B_1 = 60$ G, a pulse of sufficient intensity to excite most of the spins in the sample, and the duration of the finite pulses $t_p = 65$ ns, corresponding to the maximum coherence efficiencies for both $T_{0 \rightarrow 2}$ and $T_{2 \rightarrow -1}$ are used for all simulations. All other parameters used for the simulations are listed in Table 1. Relaxation is not considered in these simulations.
- (iii) The coherence transfer efficiency $T_{0 \rightarrow 2}$ calculated analytically using expression (31) for weak irradiation microwave field, $B_1 \leq 5$ G are plotted in Figs. 6 (a₁), (b₁), (c₁), (d₁), respectively, for the dipolar coupling constants $d = 20$ MHz, $d = 30$ MHz, $d = 40$ MHz and $d = 50$ MHz. For comparison, the same simulations are carried out numerically without

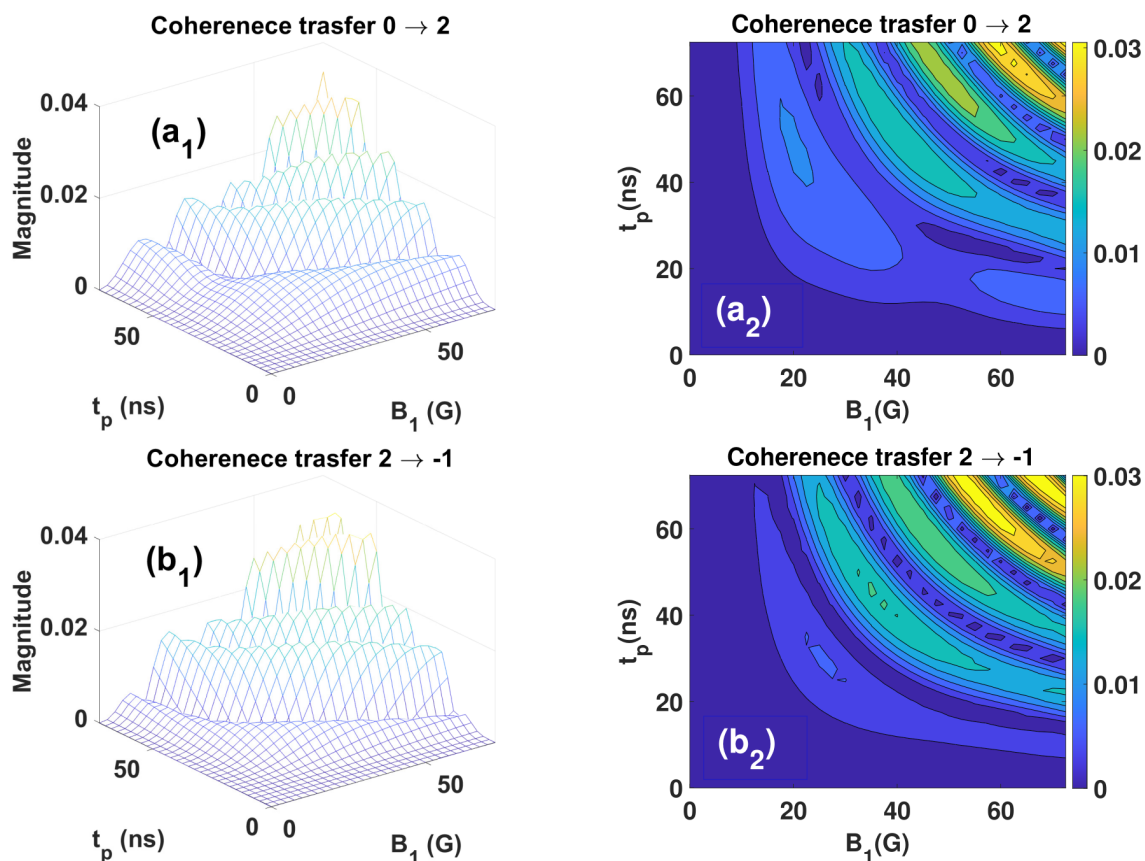


Figure 8. Two-pulse DQ coherence transfers for a polycrystalline sample, averaged over twenty Monte-Carlo orientations of the nitroxide dipoles of the biradical: (left) the absolute values and (right) their contour plots of the coherence transfers; (top) $T_{0 \rightarrow 2}$ and (bottom) $T_{2 \rightarrow -1}$, as functions of the intensity of the irradiation microwave magnetic pulse, B_1 and the duration of the pulses, t_p for the dipolar coupling constant $d = 10$ MHz. All the parameters used for simulations are the same as those listed in Table 1. It is seen from these simulations that for $B_1 = 60$ G and $t_p = 65$ ns, which are experimentally feasible values, a maximum coherence transfer is achieved for both $0 \rightarrow 2$ and $2 \rightarrow -1$ transitions. These (B_1, t_p) values are used for the calculation of the DQ signal, shown in Fig. 4.

neglecting any terms in the spin Hamiltonian. The results are plotted in Figs. 6 (a₂), (b₂), (c₂), (d₂). The duration of the pulse t_p is chosen to produce a nominal $\pi/2$ pulse in each case. A grid of 180×180 points of (θ, ϕ) with 20 sets of random Euler angles were used in the calculations. All the other parameters are the same as those listed in Table 1. It is seen that the intensity of the coherence transfer $T_{0 \rightarrow 2}$ is maximum for those coupled nitroxides, whose dipolar axes are oriented about $\pm 10^\circ$ away from the magic angle $\theta_0 \approx 54.74^\circ$, at which $(3 \cos^2 \theta - 1) = 0$, for $0^\circ \leq \theta \leq 90^\circ$, being symmetric about $\theta = 90^\circ$ in the range $0^\circ \leq \theta \leq 180^\circ$, implying that these spins will be preferentially pumped from $p = 0$ to $p = 2$ coherence state. The analytical and rigorous numerical calculations are found to be in very good agreement with each other, justifying the validity of the analytical expressions (31) and (32).

- (iv) The effect of relaxation on the DQ signal is shown in Fig. 7, displaying the Fourier transform of the DQ signal without and with relaxation. The latter is calculated with the relaxation times $T_2^S = 500$ ns (over the pathways $p = \pm 1$) and $T_2^D = 200$ ns (over the pathways $p = \pm 2$), $d = 40$ MHz and $B_1 = 10.0$ G. As expected, the Pake doublets do become broadened

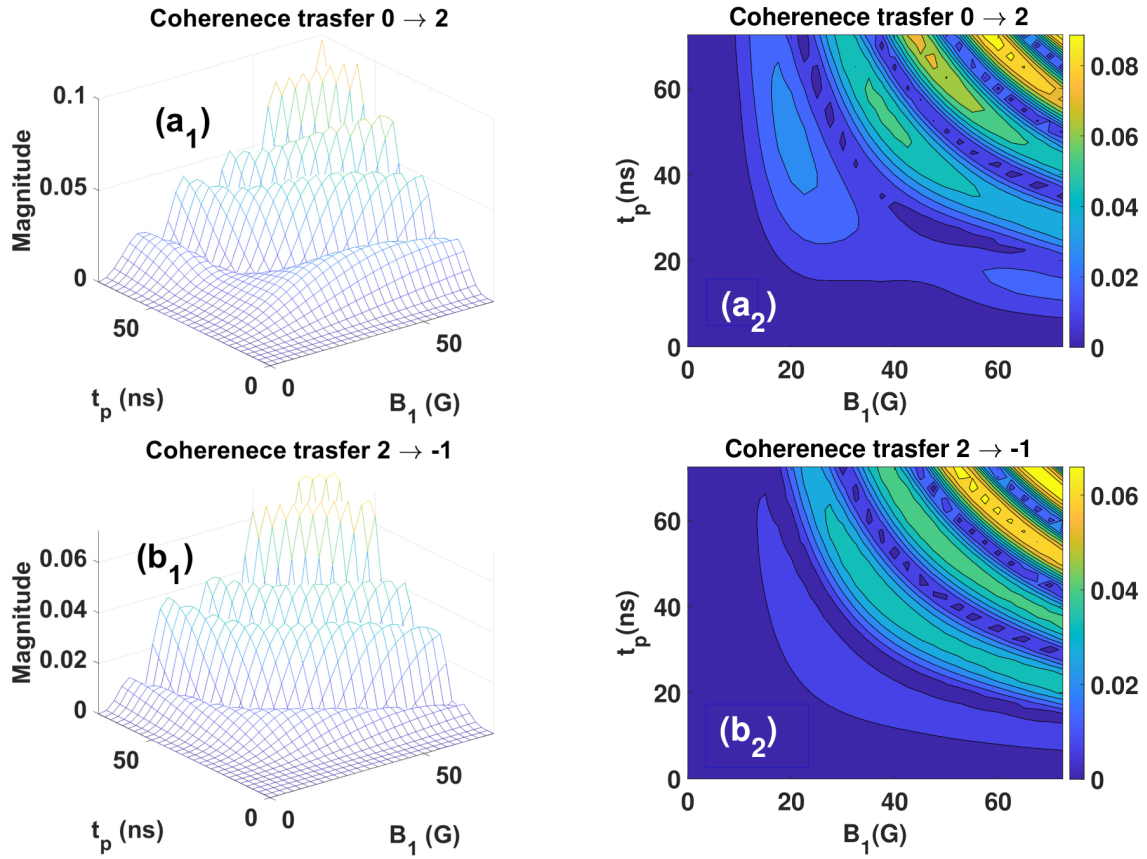


Figure 9. The same details as those for Fig. 8, except that here the simulations are for the dipolar coupling constant $d = 20$ MHz

by relaxation. Furthermore, T_2^D is found to make more dominant contribution as compared to that of T_2^S , since its value is almost half that of T_2^S as determined experimentally in [28], considering the relaxations factors, which are inversely proportional to the exponential of the relaxation time.

- (v) The efficiencies of the coherence transfers for the transitions $0 \rightarrow 2$ and $2 \rightarrow -1$ in the DQ two-pulse experiment are plotted in Figs. 8, 9 and 10 as functions of (B_1, t_p) for the values of the dipolar constant $d = 10, 20$ and 30 MHz, respectively. They show that the value of the coherence transfer in the DQ experiment for the transition $0 \rightarrow 2$ is about the same as that for the transition $2 \rightarrow -1$. Furthermore, coherence transfers are found to be significantly affected by the dipolar interaction; specifically, the efficiency of the coherence transfer in the transition $0 \rightarrow 2$ increases from 0.03 for $d = 10$ MHz to 0.12 for $d = 30$ MHz.

8.2. Five-pulse DQM signal

The relevant features of the simulations for the coherence transfer for the DQM signal are as follows.

- (i) The time-domain DQM signals, simulated for $t_5 = t_1$ for the dipolar constants $d = 0.5, 7, 10, 20, 30, 40, 50$ MHz, are shown in Figs 11 (a₁), (b₁), (c₁), (d₁), (e₁), (f₁), (g₁), respectively, as functions of t_5 . The corresponding Fourier transforms of these signals are shown in Figs 11 (a₂), (b₂), (c₂), (d₂), (e₂), (f₂), (g₂), respectively; Those shown in black are taken with respect to t_5 , whereas those in blue are taken with respect to the

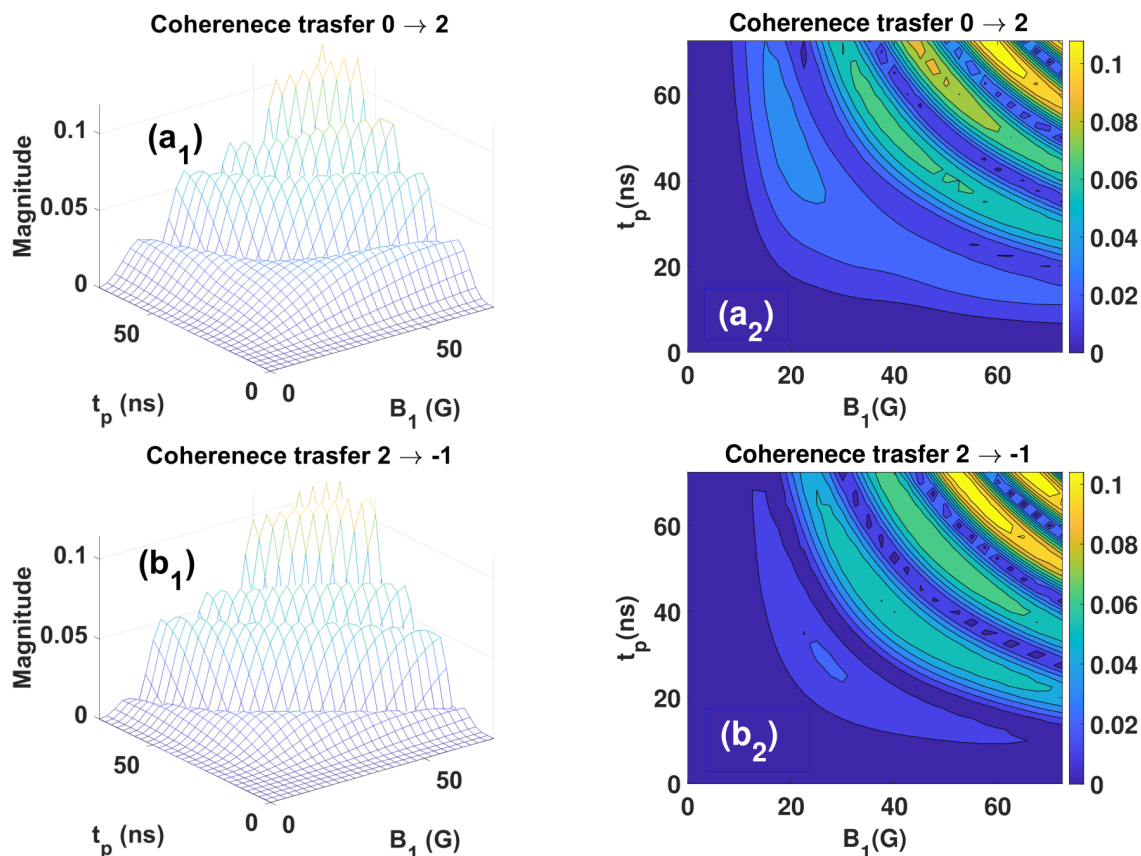


Figure 10. The same details as those for Fig. 8, except that here the simulations are for the dipolar-coupling constant $d = 30$ MHz

reduced echo time, $(t_5 - t_d)$, the time period over which the signal can be recorded. The Pake doublets in the Fourier transforms of the DQM signals, indeed, appear at $\pm d$, for the transform taken with respect to t_5 in accordance with that deduced theoretically in Sec. 2.5.2. It is seen that the Fourier transform taken with respect to the reduced echo time, $(t_5 - t_d)$ does not distort the Pake doublets, or its position. It reduces only the intensity and the width of the Fourier transform. Furthermore, the relative intensities of the side peaks with respect to the main peaks at $\pm d$, are also somewhat reduced. The values of the parameters used are: $B_1 = 17.8$ G, the same as that used at X-band in [28], the durations of the pulses: $(t_p)_1 = (t_p)_3 = (t_p)_5 = 5$ ns, $(t_p)_2 = (t_p)_4 = 10$ ns, $t_d = 35$ ns, as used experimentally in [3] at X-band. The initial time domain signals during the 35 ns interval, lost in the dead-time of the pulse, is shown as hatched.

- (ii) The effect of relaxation on the DQM signal is shown in Figs. 12 (a) and (b), respectively, displaying the Fourier transform of the DQM signal without and with relaxation. The latter is calculated for the relaxation times $T_1 = 10 \mu\text{s}$ (over the pathway $p = 0$), $T_2^S = 500$ ns (over the pathways $p = \pm 1$) and $T_2^D = 200$ ns (over the pathways $p = \pm 2$), using the stretching parameter $\beta = 0.8$, $d = 40$ MHz and $B_1 = 17.8$ G. As expected, the Pake doublets become broadened by relaxation. The relaxation times T_1 and T_2^S contribute to this broadening in the frequency domain, whereas T_2^D does not have any effect on the broadening of the peaks, since it operates over a constant time, reducing only the intensity. Furthermore, T_2^S has more dominant contribution as compared to that of T_1 , since the relaxations factors are inversely proportional to the exponential

of the relaxation time.

- (iii) Figure 13 shows the simulation of the five-pulse DQM signal of the nitroxide biradical to fit the experimental data obtained by Saxena and Freed [28]. The simulations are carried out, using the same parameters as those listed in [28], employing the numerical algorithm as given above in Secs. 4 and 6. The experimental data shown here is a profile of the maximum of the intensity that occurs for $t_5 = t_1$ of the intensity versus (t_5, t_1) data, reported in [28]. The parameters used for the simulation are the same as that used in [28], which are specifically: $B_1 = 17.8$ G; $d = 12.3$ MHz, $T_2^S = 500$ ns, $T_2^D = 300$ ns; $(t_p)_1 = (t_p)_3 = (t_p)_5 = 5$ ns and $(t_p)_2 = (t_p)_4 = 10$ ns. The other parameters are the same as those listed in Table 1. The simulation shows a reasonably good agreement, within experimental errors, to the experiment [28].

8.3. Two-pulse DQ and five-pulse DQM at Ku-band

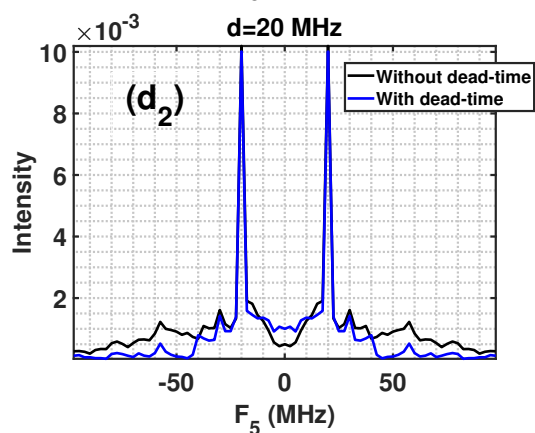
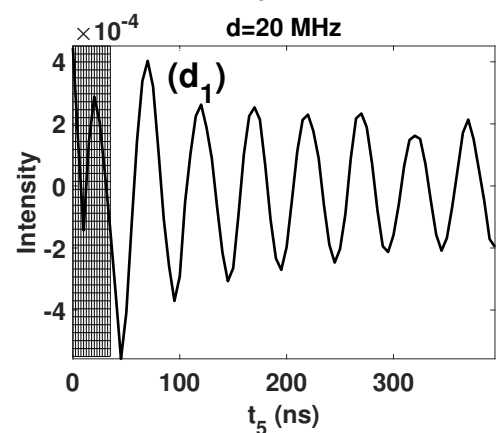
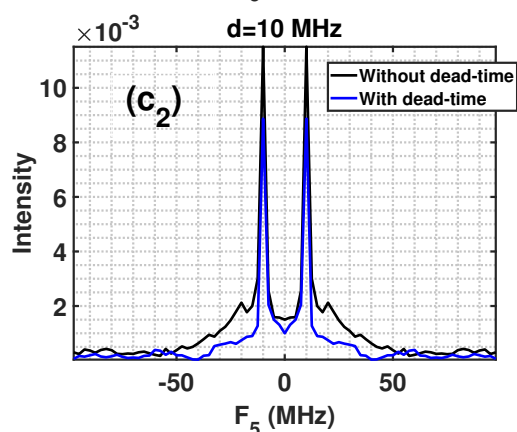
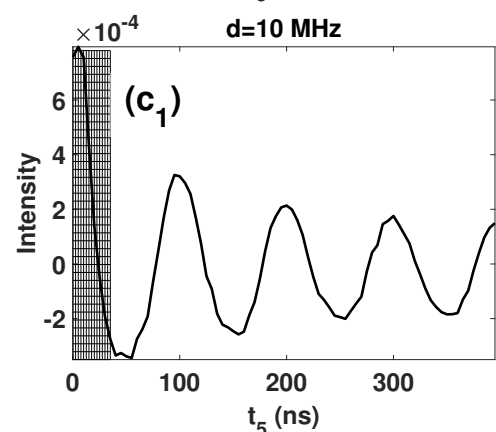
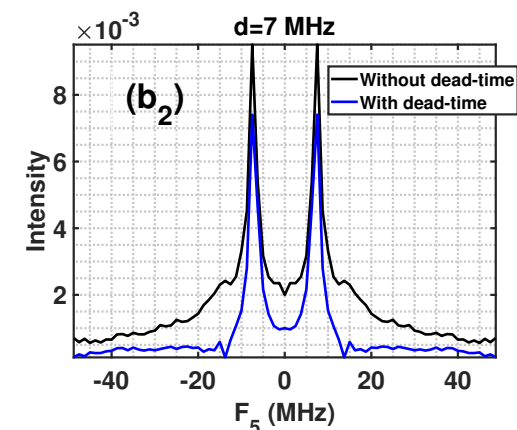
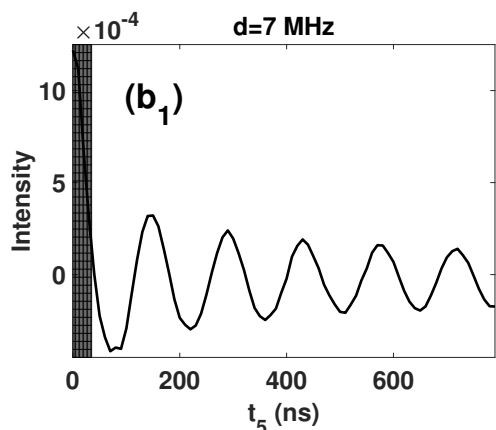
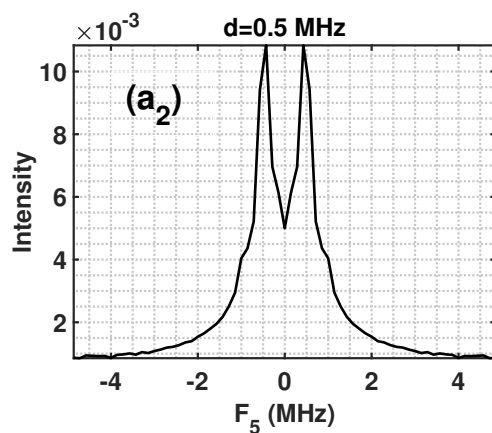
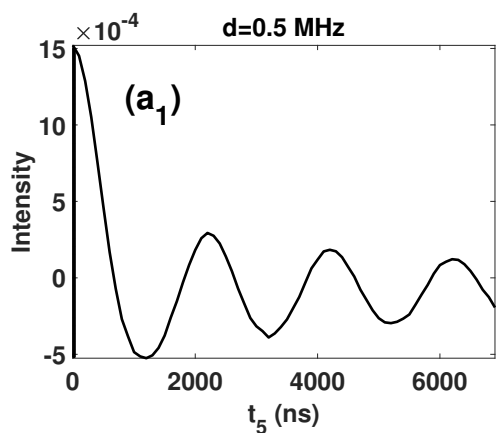
The two pulse DQ and five pulse DQM signals at Ku-band are plotted in Fig. 14, along with their Fourier transforms. The same parameter as those used for the simulation of two-pulse DQ and five-pulse DQM signals in Figs. 4(c₁) and 11(c₁), respectively, are used for the simulation at Ku-band except that here $B_0 = 6200$ G. The dead-time of 25 ns is used at Ku-band in accordance with the experiment [3]. The initial 25 ns interval of the time domain signals covered by the dead time of the pulse, which cannot be recorded in the experiment, is shown as hatched. The Fourier transforms shown in blue are taken with respect to the reduced times $t_2 - t_d$ and $t_5 - t_d$, where t_d is the dead time, whereas those in black are taken with respect to t_2 and t_5 for two-pulse DQ (Fig. 14(a₂)) and five-pulse DQM (Fig. 14(b₂)), respectively. The Pake doublets in two-pulse DQ and five-pulse DQM at Ku-band appear at $\pm 3d/4$ and $\pm d$, respectively, the same as that at X-band. It is noted that the intensities of the signals and their respective amplitudes of Fourier transforms are larger at Ku-band as compared to those at X-band.

The numerical simulation for the coherence transfer $T_{0 \rightarrow 2}$ as function of θ , were also carried out at Ku-band (not included here) and there was found absence of orientational selectivity, i.e., the coherence transfer is not especially large for any range of θ values, unlike that at X-band (Fig. 6).

9. Conclusions

The salient features of the present numerical study of two-pulse DQ and five-pulse DQM signals and their Fourier transforms (Pake doublets) for distance measurements at X-band are as follows.

- It is shown here, from general considerations, that both the dipolar interaction and a finite pulse are needed to produce non-zero coherence transfers in the transitions $0 \rightarrow 2$ and $2 \rightarrow -1$ for both the two-pulse DQ and five-pulse DQM sequences.
- The simulations show the following features for the orientational selectivity of the forbidden DQ signal, as exhibited by the coherence transfer, $T_{0 \rightarrow 2}$: (a) It increases as the amplitude of the irradiation microwave pulse (B_1) decreases; (b) It is maximum for those coupled nitroxides, whose dipolar axes are oriented symmetrically, in a small region, at about $\pm 10^\circ$ away from the magic angle, 54.74° , and its supplementary angle, 125.26° , implying that these spins will be preferentially pumped from $p = 0$ to $p = 2$ coherence state. *This is a first-ever novel result, as far as orientational selectivity of two-pulse DQ and five-pulse DQM is concerned.* (c) It occurs up to a maximum value of B_1 that increases with d . These B_1 values for the occurrence of maximum are 1.5, 2.0, 3.0 and 4.0 G for $d = 20, 30, 40,$ and 50 MHz, respectively, for both, the two-pulse DQ and five-pulse DQM, sequences.



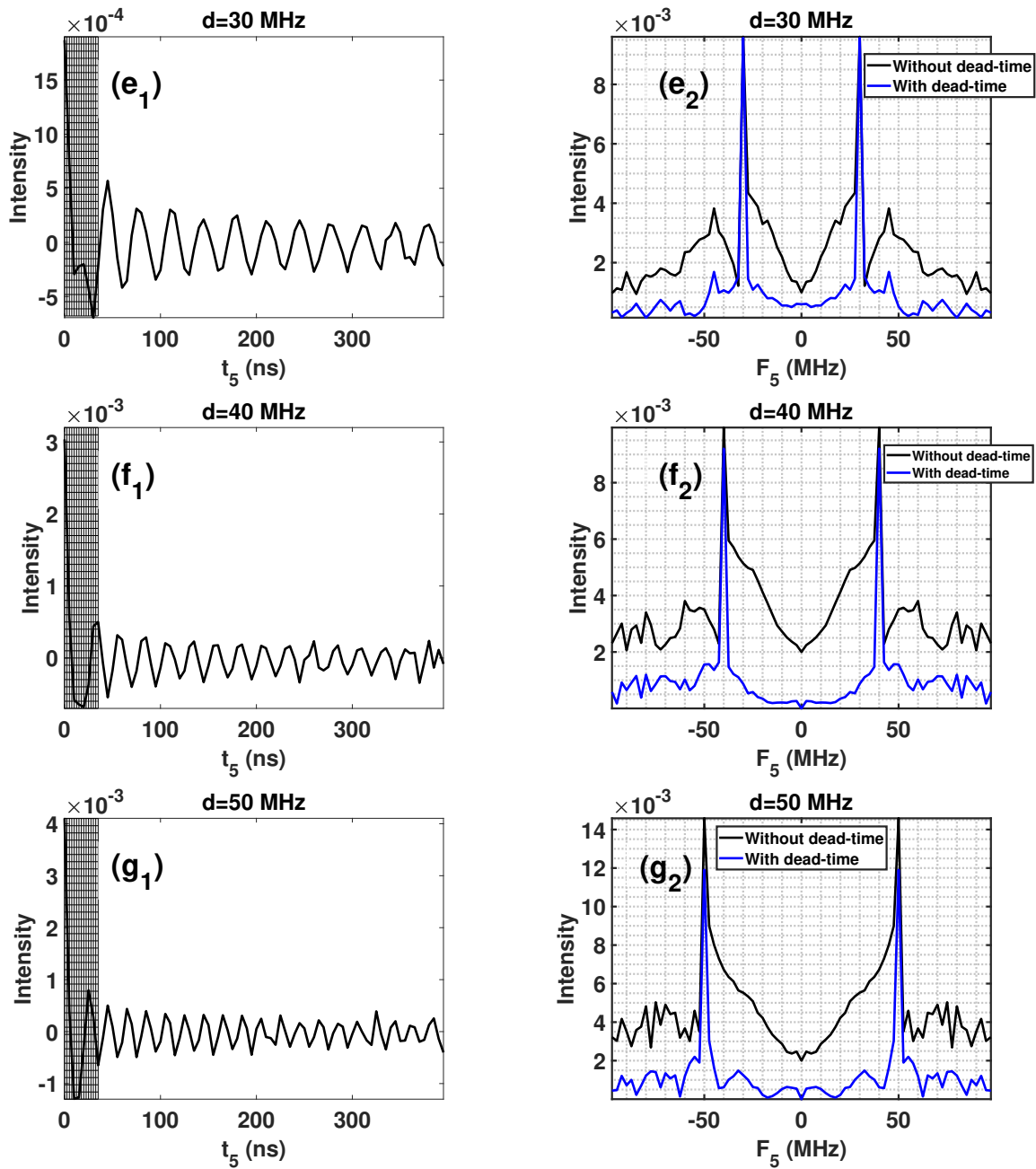


Figure 11. Dependence of the five-pulse DQM signal on dipolar coupling constant for a polycrystalline sample, averaged over twenty Monte-Carlo orientations of the nitroxide dipoles: left (a_1 , b_1 , c_1 , d_1 , e_1 , f_1 , g_1) time domain DQM signals for $t_5 = t_1$ and right (a_2 , b_2 , c_2 , d_2 , e_2 , f_2 , g_2) their Fourier transforms (Pake doublets) for $d = 0.5, 7.0, 10, 20, 30, 40, 50$ MHz. The amplitude of the irradiation microwave pulse $B_1 = 17.8$ G and the duration of the finite pulses $(t_p)_1 = (t_p)_3 = (t_p)_5 = 5$ ns ($\pi/2$ pulses) and $(t_p)_2 = (t_p)_4 = 10$ ns (π pulses) ns are used for all simulations. All other parameters used for the simulations are the same as those listed in Table 1. The relaxation is not considered in these simulations. The dead-time of $t_d = 35$ ns, as used experimentally in [3], at X-band is used. The initial 35 ns interval of the time domain signals, included in the dead-time of the pulse, is shown as hatched; it cannot be recorded in the experiment. The Fourier transform shown in blue is taken with respect to $t_5 - t_d$ whereas that in black is taken with respect to t_5 . All Pake doublets appear at $\pm d$.

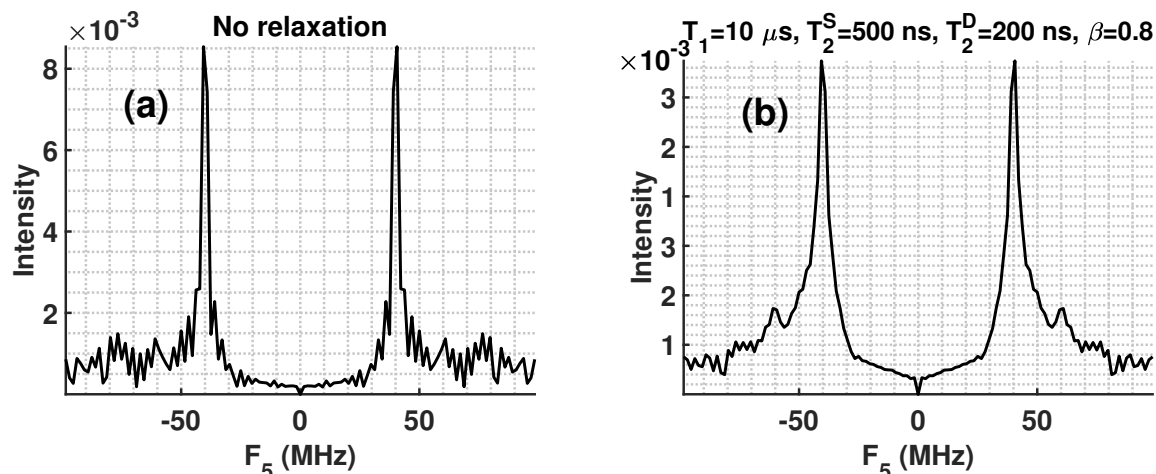


Figure 12. Effect of relaxation on the DQM signal for a polycrystalline sample, averaged over twenty Monte-Carlo orientations of the nitroxide dipoles. The Fourier transform as a function of t_1 of the time domain DQM signal at $t_5 = t_1$ is calculated for: (a) without taking relaxation into account and (b) with relaxation included for $T_2^S = 500$ ns and $T_2^D = 200$ ns using the stretching parameter $\beta = 0.8$. The dipolar coupling constant $d = 40$ MHz and the amplitude of the irradiation microwave pulse $B_1 = 17.8$ G are used in these simulations. The values of all the other parameters used in the simulations are the same as those listed in Table 1. Due to relaxation, the peaks are broadened, and the intensity of the calculated Fourier transform of the DQM signal is reduced by a factor of three in Fig. 12(b).

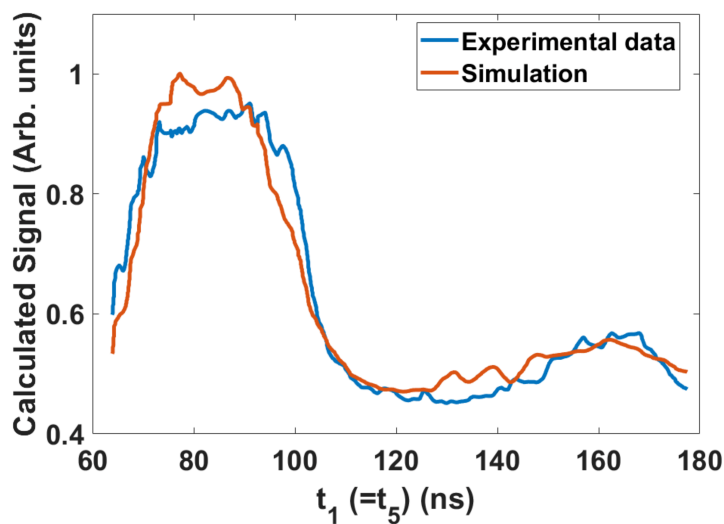


Figure 13. The simulation made using the numerical algorithm of Secs. 4 and 6 to fit the experimental five-pulse DQM signal of the nitroxide biradical [28]. The experimental data shown is a profile of the three-dimensional experiment along the maximum slice at $t_5 = t_1$ reported in [28]. The simulation parameters are: $B_1 = 17.8$ G, $d = 12.3$ MHz, $T_2^S = 500$ ns, $T_2^D = 300$ ns. The duration of the pulses is: $(t_p)_1 = (t_p)_3 = (t_p)_5 = 5$ ns and $(t_p)_2 = (t_p)_4 = 10$ ns. The other parameters are the same as those listed in Table 1. The simulation shows a reasonably good agreement with the experimental data, within experimental error.

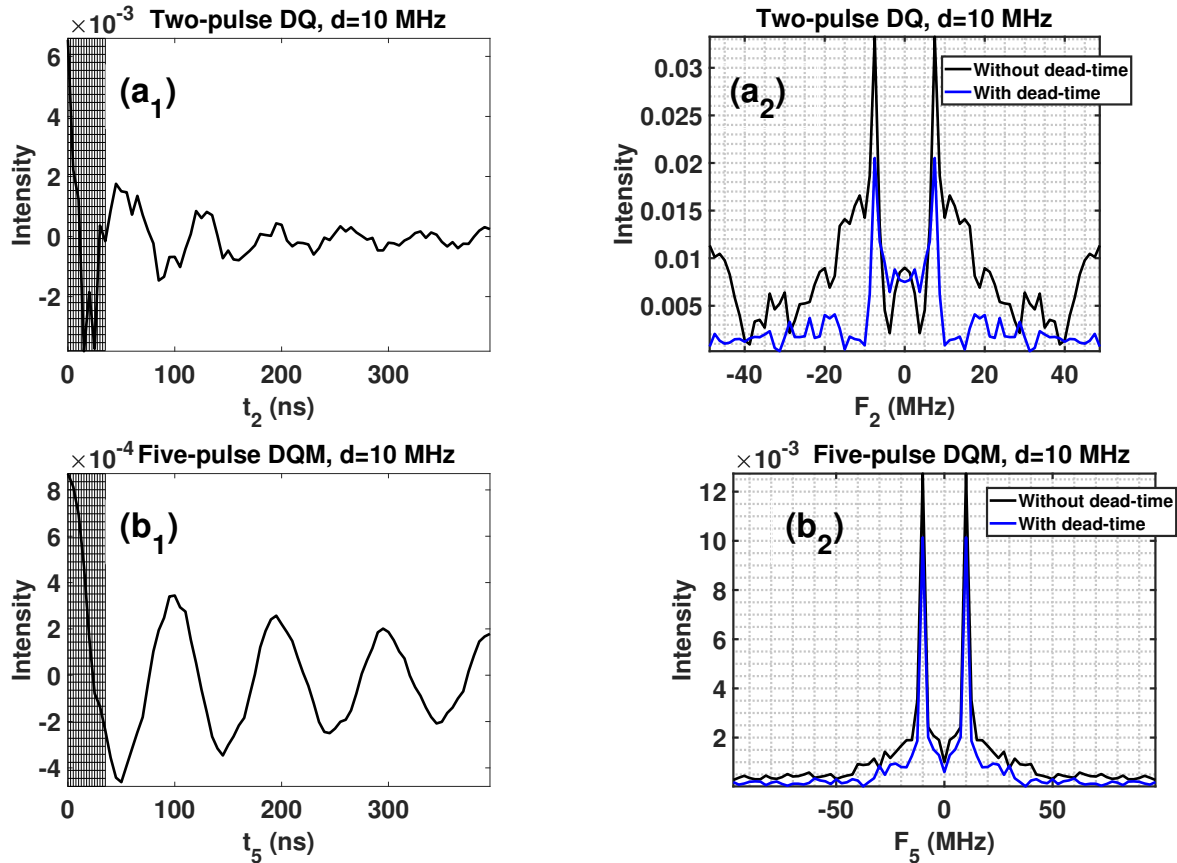


Figure 14. The two pulse DQ and five pulse DQM signals at *Ku*-band for a polycrystalline sample, averaged over twenty Monte-Carlo orientations of the nitroxide dipoles: left (a₁) time domain DQ signal for $t_2 = 2t_1$; (b₁) time domain DQM signal for $t_5 = t_1$ and right (a₂, b₂) their Fourier transforms (Pake doublets) for $d = 10$ MHz. For simulation of DQ signal, the amplitude of the irradiation microwave pulse was $B_1 = 60$ G and the duration of the finite pulses t_p for both pulses was 65 ns, whereas for the simulation of five-pulse DQM signal $B_1 = 17.8$ G and the duration of the finite pulses $(t_p)_1 = (t_p)_3 = (t_p)_5 = 5$ ns ($\pi/2$ pulses) and $(t_p)_2 = (t_p)_4 = 10$ ns (π pulses) ns are used. All other parameters used for the simulations are the same as those listed in Table 1. The relaxation is not considered in these simulations. The dead-time is $t_d = 25$ ns [3]. The initial 25 ns interval of the time domain signals, buried in the dead-time of the pulse, is shown as hatched; it cannot be recorded in the experiment. The Fourier transforms shown in blue are taken with respect to the reduced times i.e., $t_2 - t_d$ (a₂) and $t_5 - t_d$ (b₂) whereas those in black are taken with respect to t_2 and t_5 for two-pulse DQ and five-pulse DQM, respectively.

- The relaxation time over the double-quantum coherence pathway, T_2^D , can be measured with the two-pulse DQ experiment. Furthermore, the DQM experiment enables also the measurement of the spin-lattice relaxation time, T_1 , knowing T_2^D from DQ and T_2^S from a COSY (Correlation Spectroscopy) experiment [38].
- For the purpose of distance measurement, it is shown here that one needs to perform only one-dimensional time-dependent experiments, requiring measurement of the signal for only one value of the echo time, i.e., for $t_2 = 2t_1$ for two-pulse DQ and $t_5 = t_1$ for five-pulse DQM sequences.
- The Pake doublets occur at $\pm 3d/4$ and $\pm d$ for the two-pulse DQ and five-pulse DQM sequences in the polycrystalline averages, respectively, as determined from the Fourier

Coherence transfer and distance measurements

transforms of their time-dependent signals calculated with respect to the respective echo times ($t_{echo} = t_2$ or t_5) and the reduced echo times ($t_{echo} - t_d$), where t_d is the dead-time. The latter is useful even if a part of the initial signal is lost in the dead-time after the second pulse. They are thus direct measures of the dipolar interaction, from which the distance between the two nitroxide dipoles in the biradical used as spin probe, can be determined.

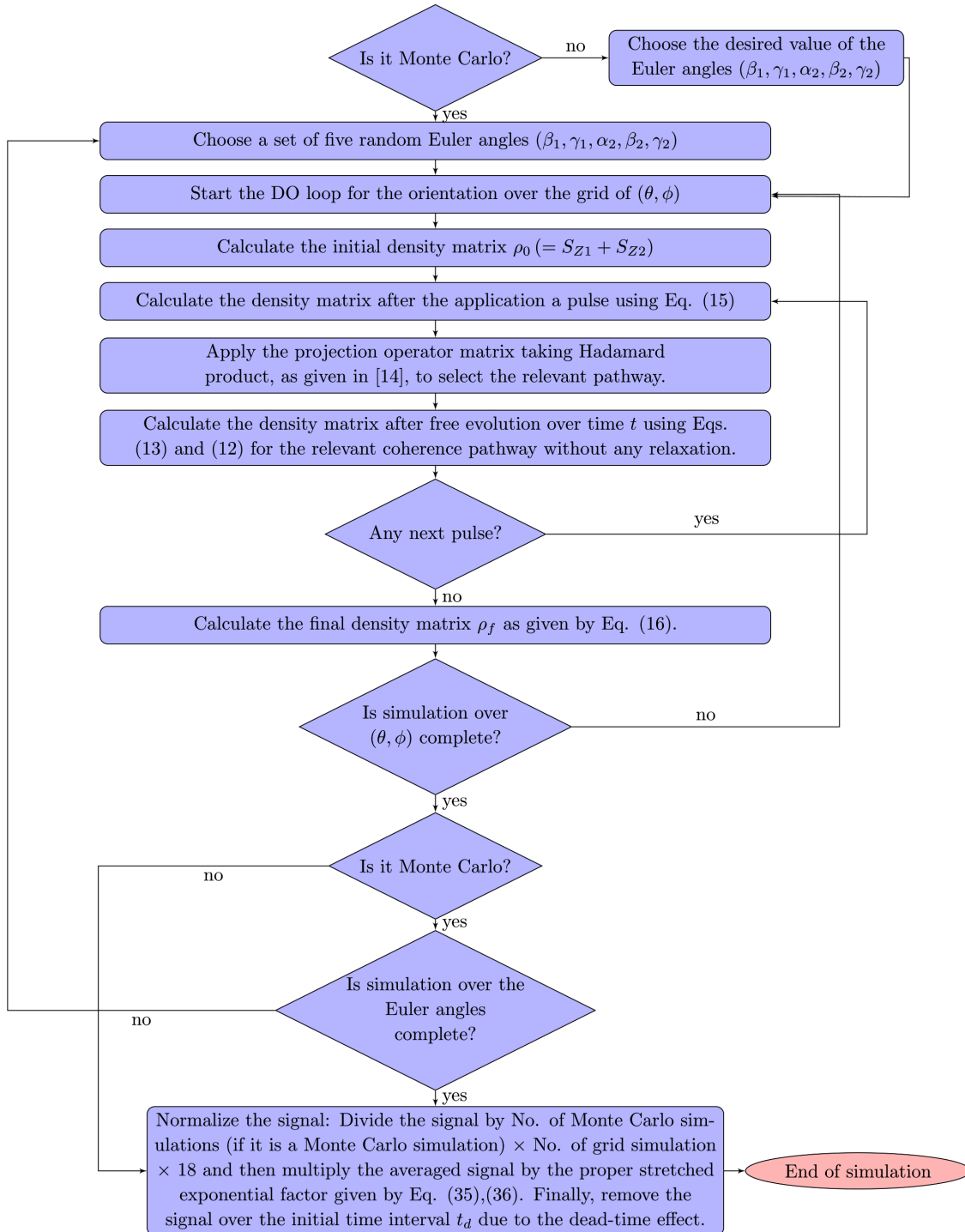
- The simulation of the five-pulse DQM signal calculated using the numerical algorithm described here shows a very good agreement with the published experimental data.
- For $d = 0.5$ MHz, for which the modulation depth, Δ , can be measured considering the dead-time effect, Δ is almost 100%, for both DQ and DQM sequences. It implies that the DQ and DQM sequences are very efficient for distance measurements, as compared with other techniques. Calculations for pulsed EPR at other bands, e.g., Ku-band (≈ 17.3 GHz) can be made in a similar fashion to that illustrated here for X-band.

Acknowledgments

We are grateful to the Natural Sciences and Engineering Council of Canada for partial financial support.

Appendices

A. Flowchart for the calculation of DQ and DQM signals



B. Five-pulse DQM signal: the M_i terms

In this Appendix, the M_i , $i = 1, \dots, 4$ terms used in the analytical expression of five-pulse DQM signal in Eqs. (21) and (22) are provided

$$M_1 = P_{12}^{(2)} + P_{13}^{(2)}, \quad M_2 = P_{42}^{(2)} + P_{43}^{(2)}, \quad M_3 = P_{22}^{(2)} + P_{23}^{(2)}, \quad M_4 = P_{32}^{(2)} + P_{33}^{(2)}. \quad (\text{B.1})$$

References

1. Saxena S., Freed J. H., *J. Chem. Phys.* **107**, 1317 (1997).
2. Misra S. K., Borbat P., Freed J. H., *Appl. Magn. Reson.* **36**, 237 (2009).
3. Borbat P., Freed J. H., *Chem. Phys. Lett.* **313**, 145 (1999).
4. Borbat P. P., Freed J. H., *EPR newsletter* **17**, 21 (2007).
5. Raitsimring A. M., Salikhov K. M., *Bull Magn Reson* **7**, 184 (1985).
6. Milov A. D., Salikhov K. M., Shirov M. D., *Sov. Phys. Solid State* **23**, 565 (1981).
7. Salikhov K. M., Dzuba S. A., Raitsimring A. M., *J. Magn. Reson.* **42**, 255 (1969).
8. Milov A. D., Salikhov K. M., Tsvetkov Y. D., *Phys. Solid State* **15**, 802 (1973).
9. Milov A. D., Tsvetkov Y. D., Formaggio F., Crisma M., Toniolo C., Raap J., *J. Am. Chem. Soc* **122**, 3843 (2000).
10. Milov A. D., Tsvetkov Y. D., Formaggio F., Crisma M., Toniolo C., Raap J., *J. Am. Chem. Soc* **123**, 3784 (2001).
11. Milov A. D., Tsvetkov Y. D., Formaggio F., Oancea S., Toniolo C., Raap J., *J. Phys. Chem. B* **107**, 13719 (2003).
12. Milov A. D., Naumov B. D., Tsvetkov Y. D., *Appl. Magn. Reson.* **26**, 587 (2004).
13. Milov A. D., Tsvetkov Y. D., *Appl. Magn. Reson* **12**, 495 (1997).
14. Misra S. K., Salahi H. R., *Magn. Reson. Solids* **23**, 21101 (2021).
15. Ernst R., Bodenhausen G., Wokaun A., *Principles of Nuclear Magnetic Resonance in One and Two Dimensions* (Clarendon Press, Oxford, 1991).
16. Wu G., Rovnyank D., Sun B., Griffin R. B., *Chem. Phys. Lett* **249**, 449 (1996).
17. Fernandez C., Amoureux J. P., *Chem. Phys. Lett* **242**, 210 (1995).
18. Medek A., Hardwood J. S., Frydman L., *J. Am. Chem. Soc.* **117**, 12779 (1995).
19. Solomon I., *Phys. Rev.* **110**, 61 (1958).
20. Abragam A., *The Principles of Nuclear Magnetism* (Oxford University Press, New York, 1961) p. 245.
21. Murzakhanov F., Mamin G. V., Orlinskii S., Goldberg M., Petrakova N. V., Fedotov A. Y., Grishin P., Gafurov M. R., Komlev V. S., *ACS Omega* **6**, 25338 (2021).
22. Baibekov E., Kurkin I., Gafurov M., Endeward B., Rakhmatullin R., Mamin G., *J. Magn. Reson.* **209**, 61 (2011).
23. Baibekov E., Gafurov M. R., Zverev D. G., Kurkin I. N., Rodionov A. A., Malkin B. Z., Barbara B., *Phys. Rev. B* **95**, 064427 (2017).

24. Bao Z., Wang Z., Wu Y., Li Y., Ma C., Song Y., Zhang H., Duan L., *Phys. Rev. Lett.* **127**, 010503 (2021).
25. Soltamov V. A., Yavkin B. V., Anisimov A. N., Bundakova H. S. A. P., Mamin G. V., Orlinskii S. B., Mokhov E. N., Suter D., Baranov P. G., *Phys. Rev. B* **103**, 195201 (2021).
26. Moiseev S. A., Gerasimov K. I., Latypov R. R., Perminov N. S., Petrovnin K. V., Sherstyukov O. N., *Sci. Rep.* **8**, 1 (2018).
27. Maryasov A. G., Tsvetkov Y. D., *Appl. Magn. Reson* **18**, 583 (2000).
28. Saxena S., Freed J. H., *Chem. Phys. Lett.* **251**, 102 (1996).
29. Stein N., Mainali L., Hyde J. S., Subczynski W. K., *Appl. Magn. Reson* **50**, 903 (2019).
30. Pfenninger S., Antholine W. E., Barr M. E., Hyde J. S., Kroneck P. M., Zumft W. G., *Biophys. J.* **69**, 2761 (1995).
31. Itoh K., Hayashi H., Nagakura S., *Molecular Physics* **17**, 561 (1969).
32. Misra S. K., Salahi H. R., *Appl. Magn. Reson.* **52**, 247 (2021).
33. Lee S., Patyal B. R., Freed J. H., *J. Chem. Phys.* **98**, 3665 (1993).
34. Misra S. K., Salahi H. R., Li L., *Magn. Reson. Solids* **21**, 19505 (2019).
35. Raitsimring A., Borbat P., *Chem. Phys. Lett* **262**, 8 (1996).
36. Jeschke G., Koch A., Jonas U., Godt A., *J. Magn. Reson.* **155**, 72 (2002).
37. Halbmaier K., Wegner J., Diederichsen U., Bennati M., *Biophys. J.* **11**, 2345 (2016).
38. Misra S. K., Salahi H. R., *Appl. Magn. Reson.* **52**, 247 (2021).